

Hierarchical Liouville-space approach for accurate and universal characterization of quantum impurity systems

ZhenHua Li,¹ NingHua Tong,¹ Xiao Zheng,^{2,*} Dong Hou,² JianHua Wei,^{1,†} Jie Hu,^{3,4} and YiJing Yan^{2,3,‡}

¹*Department of Physics, Renmin University of China, Beijing 100872, China*

²*Hefei National Laboratory for Physical Sciences at the Microscale, University of Science and Technology of China, Hefei, Anhui 230026, China*

³*Department of Chemistry, Hong Kong University of Science and Technology, Hong Kong, China*

⁴*Department of Physics, Capital Normal University, Beijing 100048, China*

(Dated: Submitted on June 18, 2012; revised on November 23, 2012)

A hierarchical equations of motion (HEOM) based numerical approach is developed for accurate and efficient evaluation of dynamical observables of strongly correlated quantum impurity systems. This approach is capable of describing quantitatively Kondo resonance and Fermi liquid characteristics, achieving the accuracy of latest high-level numerical renormalization group approach, as demonstrated on single-impurity Anderson model systems. Its application to a two-impurity Anderson model results in differential conductance versus external bias, which correctly reproduces the continuous transition from Kondo states of individual impurity to singlet spin-states formed between two impurities. The outstanding performance on characterizing both equilibrium and nonequilibrium properties of quantum impurity systems makes the HEOM approach potentially useful for addressing strongly correlated lattice systems in the framework of dynamical mean field theory.

PACS numbers: 71.27.+a, 72.15.Qm

Quantum impurity systems cover a broad range of important physical systems where strong electron-electron (e - e) interactions among a few localized impurities affect crucially the system properties. Besides the e - e interactions, the impurities are coupled to the itinerant electrons in surrounding bulk materials, which serve as the electron reservoir and thermal bath. Moreover, some extensive strongly correlated systems can be treated as quantum impurity systems. For instance, the celebrated Hubbard model can be mapped onto an Anderson impurity system via a self-consistent dynamical mean-field theory [1]. The strong e - e interactions give rise to a variety of intriguing phenomena of prominent many-body nature, such as Kondo effects, Mott metal-insulator transition, and high-temperature superconductivity. Examples of localized impurities are the d - or f -electrons of transition metal atoms and electrons trapped in quantum dots.

Accurate characterization of quantum impurity systems is the key to the understanding of the mechanisms and effects of strong electron correlations. This has remained a very challenging task, especially for the quantitative evaluation of dynamical quantities directly related to experimental measurements, such as the projected density of states and spectral function of the localized impurities. A vast amount of theoretical efforts have been devoted to achieving this goal, including the quantum Monte Carlo (QMC) approach [2, 3], density matrix renormalization group method [4, 5], numerical renormalization group (NRG) method [6, 7], many-body perturba-

tion theory [8], effective/quasi single-particle approaches [9, 10], *etc.* Despite their success in elucidating some fundamental features of electron correlations, the practicality of existing approaches has been limited within a few basic models [11–13]. The reason is mainly twofold: (i) the applicability of involving techniques relies critically on the system configuration, and (ii) the complexity of numerical algorithms increases dramatically with the number of impurities. Consequently, generalization of existing approaches [2–7] to more complex models is often difficult. Therefore, an accurate and universal approach capable of addressing strong correlation effects in general quantum impurity systems is highly desirable.

In this Letter we propose a general approach based on a hierarchical equations of motion (HEOM) formalism [14] to characterize quantum impurity systems from the perspective of open dissipative dynamics. The localized impurities constitute the open system of primary interest, while the surrounding reservoirs of itinerant electrons are treated as environment. The total Hamiltonian consists of the interacting impurities (H_{sys}), the noninteracting electron reservoirs (H_{res}), and their couplings $H_{\text{sys-res}} = \sum_{\alpha\mu k} (t_{\alpha\mu k} \hat{a}_{\mu}^{\dagger} \hat{d}_{\alpha k} + \text{H.c.})$. Here, \hat{a}_{μ}^{\dagger} and \hat{a}_{μ} denote the creation and annihilation operators for impurity state $|\mu\rangle$ (including spin, space, *etc.*), while $\hat{d}_{\alpha k}^{\dagger}$ and $\hat{d}_{\alpha k}$ are those for the α -reservoir state $|k\rangle$ of energy $\epsilon_{\alpha k}$. The influence of electron reservoirs on the impurities is taken into account through the hybridization functions, $\Delta_{\mu\nu}(\omega) \equiv \sum_{\alpha} \Delta_{\alpha\mu\nu}(\omega) = \pi \sum_{\alpha k} t_{\alpha\mu k} t_{\alpha\nu k}^* \delta(\omega - \epsilon_{\alpha k})$, in the absence of applied chemical potentials.

*Electronic address: xz58@ustc.edu.cn

†Electronic address: wjh@ruc.edu.cn

‡Electronic address: yyan@ust.hk

The HEOM that governs the dynamics of open system

assumes the form of [14]:

$$\begin{aligned} \dot{\rho}_{j_1 \dots j_n}^{(n)} = & - \left(i\mathcal{L} + \sum_{r=1}^n \gamma_{j_r} \right) \rho_{j_1 \dots j_n}^{(n)} - i \sum_j \mathcal{A}_{\bar{j}} \rho_{j_1 \dots j_n j}^{(n+1)} \\ & - i \sum_{r=1}^n (-)^{n-r} \mathcal{C}_{j_r} \rho_{j_1 \dots j_{r-1} j_{r+1} \dots j_n}^{(n-1)}. \end{aligned} \quad (1)$$

The basic variables are the reduced system density operator $\rho^{(0)}(t) \equiv \text{tr}_{\text{res}} \rho_{\text{total}}(t)$ and auxiliary density operators, $\{\rho_{j_1 \dots j_n}^{(n)}(t); n = 1, \dots, L\}$, with L denoting the terminal or truncated tier level. The Liouvillian of impurities, $\mathcal{L} \cdot \equiv \hbar^{-1} [H_{\text{sys}}, \cdot]$, may contain both e - e interaction and time-dependent external fields. The superoperators $\mathcal{A}_{\bar{j}}$ and \mathcal{C}_j are expressed by Eq. (S1) of Ref. [15]. The index $j \equiv (\sigma \mu m)$ corresponds to the transfer of an electron to/from ($\sigma = +/ -$) the impurity state μ , associated with the characteristic memory time γ_m^{-1} . The total number of distinct j -indexes involved is determined by the preset level of accuracy for decomposing reservoir correlation functions by exponential functions. Such a number draws the maximum tier level L_{max} , at which Eq. (1) ultimately terminate [15]. The hierarchy is self-contained at $L = 2$ for noninteracting H_{sys} [14]; while for H_{sys} involving e - e interactions, the solution of Eq. (1) must go through systematic tests to confirm its convergence versus L . In practice, a relatively low L (≈ 4) is usually sufficient to yield quantitatively converged results for weak and medium impurity-reservoir couplings.

The details of the HEOM formalism are referred to Refs. [14–17]. Here, we focus on some of its key features: (i) It is based on the Feynmann–Vernon path integral formalism [18], with fermionic operators represented by Grassmann variables [19]. (ii) It resolves nonperturbatively the combined effects of impurity-reservoir dissipation, e - e interactions, and non-Markovian memory [14]. (iii) The influence of reservoir environment on physical properties of impurities is taken into account via the hybridization functions, which enter Eq. (1) through a recently developed optimal Padé spectrum decomposition scheme [20, 21]. (iv) Besides the equilibrium dynamical observables, it is also capable of addressing nonequilibrium response of quantum impurity systems to external fields such as laser pulses or applied voltages [17].

The HEOM approach has been applied to study static and transient electron transport through quantum dot systems, with which some interesting phenomena have been revealed, such as the dynamical Coulomb blockade [22] and dynamical Kondo transition [16].

In the framework of HEOM, there are two schemes to evaluate the dynamical observables of quantum impurity systems. (i) Calculate relevant system correlation/response functions based on an HEOM-space linear response theory [15]. The correlation function for two arbitrary system operators \hat{A} and \hat{B} is $\tilde{C}_{AB}(t) \equiv \langle \hat{A}(t) \hat{B}(0) \rangle = \text{tr}_{\text{total}} [\hat{A}(t) \hat{B}(0) \rho_{\text{total}}^{\text{eq}}(T)]$, where $\rho_{\text{total}}^{\text{eq}}(T)$ is the equilibrium density operator of the total system. $\tilde{C}_{AB}(t)$ can be evaluated by using the quan-

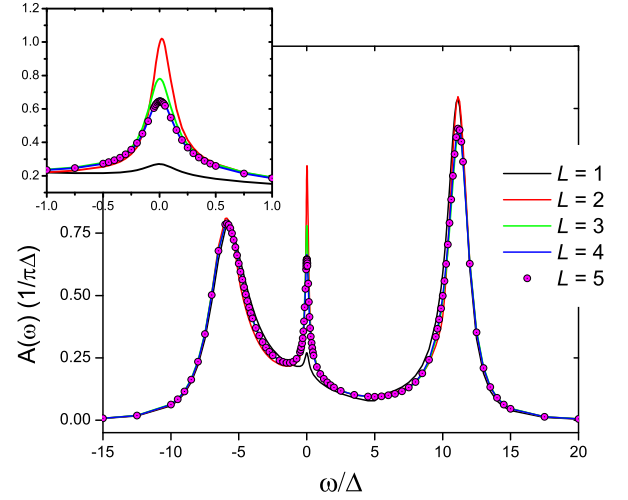


FIG. 1: (Color online). The spin-up or down spectral function of an asymmetric SIAM calculated by the HEOM approach at different truncation tiers. The inset magnifies the Kondo resonance peak at $\omega = 0$. The parameters adopted are $\epsilon_d = -5$, $U = 15$, $W = 10$, and $T = 0.075$ (in unit of Δ).

tum Liouville propagator in the HEOM space [15]. Let $C_{AB}(\omega) \equiv \frac{1}{2} \int dt e^{i\omega t} \tilde{C}_{AB}(t)$, which satisfies the detailed balance relation of $C_{BA}(-\omega) = e^{-\omega/k_B T} C_{AB}(\omega)$. The corresponding spectral function is $J_{AB}(\omega) \equiv \frac{1}{2\pi} \int dt e^{i\omega t} \langle \{\hat{A}(t), \hat{B}(0)\} \rangle = \frac{1}{\pi} (1 + e^{-\omega/k_B T}) C_{AB}(\omega)$. In particular, with $\hat{A} = \hat{B}^\dagger = \hat{a}_\mu$, $J_{\hat{a}_\mu \hat{a}_\mu^\dagger}(\omega) = A_\mu(\omega)$ gives the spectral density of impurity state μ , which can be measured experimentally via angle-resolved photoemission spectroscopy [23] and scanning tunneling microscope [24]. (ii) Solve Eq. (1) for nonequilibrium electronic response under external perturbation. For instance, the differential conductance (dI/dV) can be calculated via the response current under applied bias, followed by a finite difference analysis. The above two schemes are completely equivalent for linear response properties.

It is emphasized that the HEOM approach is distinctly different from the conventional equations of motion (EOM) method using many-body Green's functions (GFs) as basic variables [25]. The GF–EOM method often treats the impurities and reservoirs on equal footing. To close the equations it invokes specific approximations for individual GFs. In contrast, the HEOM approach focuses on the impurities, with all reservoir degrees of freedom averaged out properly [14]. Consequently, the HEOM involve much fewer unknowns than GF–EOM at same tier level. Moreover, the generic form of Eq. (1) applies to any complex impurity system, without additional derivation effort. Therefore, the HEOM approach outperforms GF–EOM in terms of both efficiency and universality [15].

For numerical demonstrations, consider first an asymmetric single-impurity Anderson model (SIAM) system that has been widely studied [26]. $H_{\text{sys}} = \epsilon_d(\hat{n}_\uparrow + \hat{n}_\downarrow) + U\hat{n}_\uparrow\hat{n}_\downarrow$, where $\hat{n}_\mu = \hat{a}_\mu^\dagger \hat{a}_\mu$ and $U \neq -2\epsilon_d$. Lorentzian

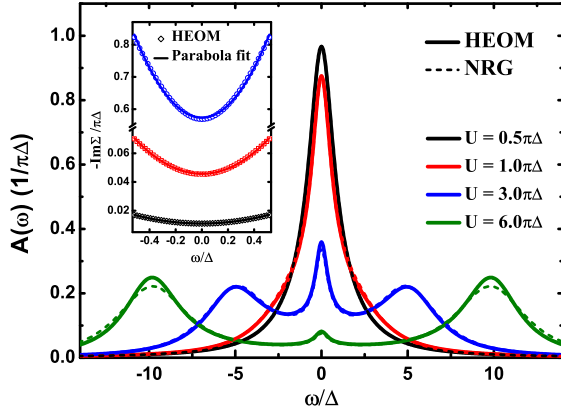


FIG. 2: (Color online). Comparison between $A(\omega)$ of symmetric SIAM calculated by HEOM and NRG methods. The parameters adopted are $T = 0.2$ and $W = 50$ (in unit of Δ). The inset shows the imaginary part of interaction self-energy calculated from HEOM at energy close to $\omega = 0$.

hybridization functions, $\Delta_{\mu\nu}(\omega) = \delta_{\mu\nu} \Delta W^2 / (\omega^2 + W^2)$, are adopted, with Δ being the effective impurity-reservoir coupling strength and W the reservoir band width. Figure 1 depicts the calculated impurity spectral function $A(\omega)$ by the HEOM approach, up to the converged tier level. The well-known spectral features of SIAM are clearly resolved: (i) The two resonance peaks at around $\omega = \epsilon_d$ and $U + \epsilon_d$ correspond to the excitation energies associated with change of impurity occupancy state. (ii) The peak at the Fermi energy ($\omega = E_F \equiv 0$) highlights the presence of Kondo resonance under a low temperature. (iii) The sum rule $\int A(\omega) d\omega = 1$ is satisfied to numerical precision. The comparison in Fig. 1 demonstrates distinctly that the HEOM results converge rapidly with L for full energy range. This confirms that the HEOM results converge quantitatively at a relatively low truncation level, even in the Kondo regime.

Figure 2 depicts the calculated $A(\omega)$ of a symmetric ($U = -2\epsilon_d$) SIAM, from weak ($U = 0.5\pi\Delta$) to strong ($U = 6\pi\Delta$) e - e interactions. For comparison, we also show results obtained by using the full density matrix NRG method [27], where a self-energy scheme of Ref. [28] is employed, and the results are averaged over 8 different logarithmic discretizations [29]. Note that our NRG data in Fig. 2 differ slightly from those in Ref. [30], due to different $\Delta_{\mu\nu}(\omega)$ used (Lorentzian versus constant). Apparently, the two sets of curves agree quantitatively at all values of U studied. In the weak ($U = 0.5$ and $1.0\pi\Delta$) and intermediate ($U = 3\pi\Delta$) interaction regimes, HEOM and NRG curves almost overlap with each other; while in the strong ($U = 6\pi\Delta$) interaction regime minor deviation is observed in the height of Hubbard peaks, which is possibly due to remaining uncertainty in NRG results [15]. Therefore, such a benchmark comparison clearly affirms that the HEOM approach achieves the same level of accuracy as the latest high-level NRG method.

Highlighted in the inset of Fig. 2 are the imaginary part

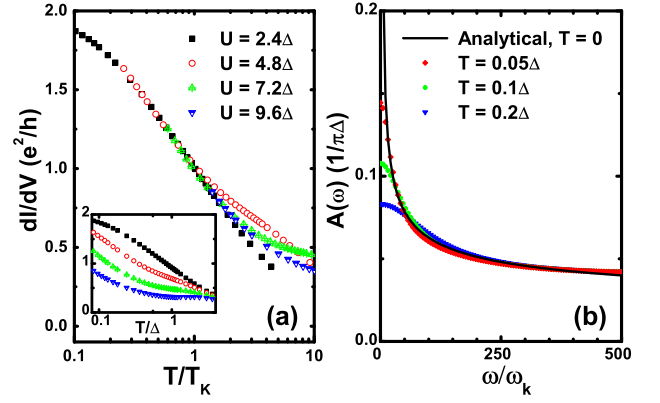


FIG. 3: (Color online). (a) dI/dV versus T/T_K for symmetric SIAM with $T_K = (U\Delta/2)^{1/2} e^{-\pi U/8\Delta + \pi\Delta/2U}$ [26] and $W = 24\Delta$. The inset depicts dI/dV versus unscaled T . (b) Comparison between the HEOM numerical results and an analytical expression, Eq. (4.2) of Ref. [35], for the large- ω tail of $A(\omega)$. Other parameters adopted are (in unit of Δ): $W = 100$, $U = -2\epsilon_d = 6\pi$. See Ref. [15] for more details.

of interaction self-energy (circles), exhibiting a parabolic lineshape near $\omega = E_F \equiv 0$ (lines). This is a clear indication of Fermi liquid character [26]. Luttinger has proved that the Kondo peak height is exactly $1/\pi\Delta$ for a symmetric SIAM at $T = 0$, independent of U [31]. At finite T and U , it is expected that in general $A(\omega = 0) < 1/\pi\Delta$ [32], as exemplified by both Fig. 1 and Fig. 2.

The HEOM results exhibit the correct scaling behavior by Kondo temperature T_K [33, 34]. This is verified by the calculated dI/dV versus T/T_K as depicted in Fig. 3(a), where the universal scaling is clearly manifested at $T < T_K$ and $\Delta \ll U \ll W$. Moreover, as T is lowered, the calculated $A(\omega)$ draws progressively to an analytic curve of a logarithmic form predicted in Ref. [35]; see Fig. 3(b).

We also compare HEOM with the latest continuous time QMC (CTQMC) approach [3] on the SIAM studied in Fig. 2. Both approaches yield quantitatively consistent imaginary time GFs with a maximum relative deviation less than 5%. However, $A(\omega)$ of CTQMC suffer from non-trivial uncertainties in analytical continuation of GFs to real energies by the maximum entropy method [15]. We then extend the comparison to the exact diagonalization [36–38], the slave-boson mean-field theory [39], and the non-crossing approximation [40]. The HEOM approach is apparently much more accurate than these methods [15]. In contrast to the fact that some existing methods would encounter practical or intrinsic problems in treating certain forms of e - e interactions, the HEOM approach admits an arbitrary form of e - e interaction (including spin-flip, electron-pair hopping, and nonlocal Coulomb interaction [41]) without additional computational cost, as long as it works with the full impurities Fock space.

The computational cost (time and memory) of present HEOM approach grows rapidly with the lowered T . This is because the resolution of long-time memory requires more exponential functions, and a higher L is usually

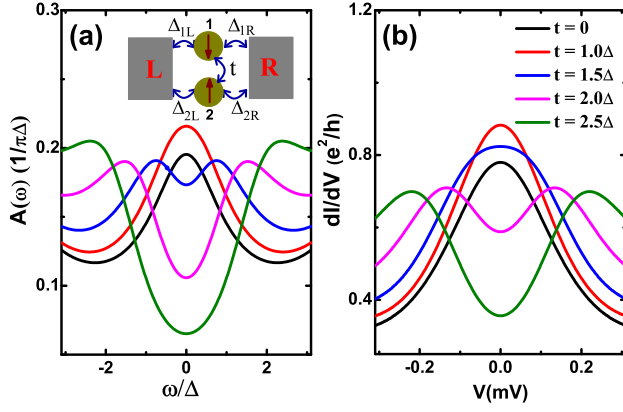


FIG. 4: (Color online). (a) $A(\omega)$ and (b) dI/dV versus V of a TIAM at various inter-impurity coupling strength ranging from 0 to 2.5Δ . The TIAM system is sketched in (a). The parameters adopted are (in unit of Δ): $W = 10$, $U_1 = U_2 = 10$, $\epsilon_1 = \epsilon_2 = -5$, and $T = 0.5$.

necessary to achieve quantitative convergence. In particular, the cost for producing $A(\omega)$ of Fig. 2 is comparable to that required for NRG and CTQMC [15]; while at a higher T , the HEOM approach would be orders of magnitude faster. Whereas at extremely low T or large Δ , the present HEOM approach may be very expensive. It is however possible to reduce the computational cost significantly by designing more efficient reservoir memory decomposition schemes.

We proceed to demonstrate that the applicability of HEOM approach can be extended beyond the simple SIAM model and equilibrium properties. To this end, a parallel-coupled two-impurity Anderson model (TIAM) sketched in Fig. 4(a) is considered, where $H_{\text{sys}} = H_1 + H_2 + V_{12}$, with H_1 (H_2) being the SIAM Hamiltonian for the impurity 1 (2), and $V_{12} = t(\hat{a}_{1\uparrow}^\dagger \hat{a}_{2\uparrow} + \hat{a}_{1\downarrow}^\dagger \hat{a}_{2\downarrow} + \text{H.c.})$. Such a TIAM model has been realized experimentally via a double quantum dot system, with the inter-dot coupling strength t tuned by plunger gates [42]. The nonzero t gives rise to an effective anti-ferromagnetic coupling, $J = 4t^2/U$, between the local spin moments at the two impurities. At a weak J , the two spin moments are nearly independent of each other, and the local spin at each impurity is screened by itinerant electrons separately. In contrast, at a sufficiently strong J , singlet spin-states covering both impurities are formed. Therefore, by varying the strength of t , the TIAM undergoes a continuous transition from Kondo singlet states of individual impurity to singlet spin-states formed between two impurities,

as confirmed by NRG and conformal-field-theory calculations [43, 44].

The HEOM approach is applied to evaluate the equilibrium spectral function $A(\omega)$ of a TIAM consisting of two identical impurities, along with its dI/dV versus external bias V . The latter is a nonequilibrium property, and is achieved via a finite difference approach [15]. The response current is extracted from first-tier ($n = 1$) auxiliary density operators [14]. Figure 4(a) and (b) depict the calculated $A(\omega) \equiv A_1(\omega) = A_2(\omega)$ and $dI/dV - V$, respectively. Apparently, the variation of $A(\omega)$ and $dI/dV - V$ with increasing t are analogous to each other. Their common features are as follows. (i) The system undergoes a transition from a Kondo singlet involving individual impurity (characterized by the single-peaked lineshape) at $t < \Delta$, to the singlet spin-state between two impurities (characterized by the double-peaked lineshape) at $t > 1.5\Delta$. (ii) The transition exhibits continuous crossover. As t increases, the single Kondo peak first broadens and approaches to its maximal height before it drops and splits into two. These features are consistent with previous experimental [42] and theoretical [43, 44] investigations.

To summarize, the practicality of our developed hierarchical Liouville-space approach is demonstrated through studies on Anderson impurity models, where the key Kondo resonance and Fermi liquid features due to strong $e-e$ interaction are accurately characterized. The HEOM approach can be straightforwardly extended to more complex quantum impurity models (such as multi-impurity models) without additional derivation and programming efforts [15]. Once converged, the HEOM results can serve as benchmarks to calibrate approximate numerical approaches, particularly the effective single-electron approaches, which are useful for studying more complex systems. Moreover, it is anticipated that HEOM would become a promising impurity solver for characterizing strongly correlated lattice systems in the framework of dynamical mean field theory [1].

The support from the Hong Kong UGC (AoE/P-04/08-2)(YJY), the NSF of China (Nos.11074302, 11074303, 21103157, 21033008, 21233007), the Fundamental Research Funds for Central Universities of China (Nos. 2340000034, 2340000025)(XZ), the Research Funds of Renmin University of China (No.11XNJ026)(JHW), and the China NKBRFSC (No. 2012CB921704)(NHT) is gratefully appreciated. We thank P. Werner, W. Wu, L. Huang, L. Du, and X. Dai for their help on CTQMC calculations.

-
- [1] A. Georges, G. Kotliar, W. Krauth, and M. J. Rozenberg, Rev. Mod. Phys. **68**, 13 (1996).
 - [2] J. E. Hirsch and R. M. Fye, Phys. Rev. Lett. **56**, 2521 (1986).
 - [3] E. Gull, et al., Rev. Mod. Phys. **83**, 349 (2011).

- [4] S. R. White, Phys. Rev. Lett. **69**, 2863 (1992).
- [5] G. Vidal, Phys. Rev. Lett. **91**, 147902 (2003).
- [6] K. G. Wilson, Rev. Mod. Phys. **47**, 773 (1975).
- [7] R. Bulla, T. A. Costi, and T. Pruschke, Rev. Mod. Phys. **80**, 395 (2008).

- [8] E. Khosravi et al., Phys. Rev. B **85**, 075103 (2012).
- [9] K. S. Thygesen and A. Rubio, Phys. Rev. B **77**, 115333 (2008).
- [10] S. Kurth, G. Stefanucci, E. Khosravi, C. Verdozzi, and E. K. U. Gross, Phys. Rev. Lett. **104**, 236801 (2010).
- [11] P. W. Anderson, Phys. Rev. **124**, 41 (1961).
- [12] J. Hubbard, Proc. Roy. Soc. A **276**, 238 (1963).
- [13] P. A. Lee, T. M. Rice, J. W. Serene, L. J. Sham, and J. W. Wilkins, Comments on Cond. Matter Phys. **12**, 99 (1986).
- [14] J. S. Jin, X. Zheng, and Y. J. Yan, J. Chem. Phys. **128**, 234703 (2008).
- [15] For details, see Supplemental Materials.
- [16] X. Zheng, J. S. Jin, S. Welack, M. Luo, and Y. J. Yan, J. Chem. Phys. **130**, 164708 (2009).
- [17] X. Zheng et al., Prog. Chem. **24**, 1129 (2012).
- [18] R. P. Feynman and F. L. Vernon, Jr., Ann. Phys. **24**, 118 (1963).
- [19] L. H. Ryder, *Quantum Field Theory*, 2nd ed., Cambridge University Press, Cambridge, 1996.
- [20] J. Hu, R. X. Xu, and Y. J. Yan, J. Chem. Phys. **133**, 101106 (2010).
- [21] J. Hu, M. Luo, F. Jiang, R. X. Xu, and Y. J. Yan, J. Chem. Phys. **134**, 244106 (2011).
- [22] X. Zheng, J. S. Jin, and Y. J. Yan, New J. Phys. **10**, 093016 (2008).
- [23] A. Damascelli, Z. Hussain, and Z. X. Shen, Rev. Mod. Phys. **75**, 473 (2003).
- [24] O. Y. Kolesnychenko et al., Phys. Rev. B **72**, 085456 (2005).
- [25] H.-G. Luo, J.-J. Ying, and S.-J. Wang, Phys. Rev. B **59**, 9710 (1999).
- [26] A. C. Hewson, *The Kondo Problem to Heavy-Fermions*, Cambridge University Press, Cambridge, 1993.
- [27] A. Weichselbaum and J. von Delft, Phys. Rev. Lett. **99**, 076402 (2007).
- [28] R. Bulla, A. C. Hewson, and T. Pruschke, J. Phys.: Condens. Matter **10**, 8365 (1998).
- [29] W. C. Oliveira and L. N. Oliveira, Phys. Rev. B **49**, 11986 (1994).
- [30] A. Isidori, D. Roosen, L. Bartosch, W. Hofstetter, and P. Kopietz, Phys. Rev. B **81**, 235120 (2010).
- [31] J. M. Luttinger, Phys. Rev. **121**, 942 (1961).
- [32] K. Yamada, Prog. Theor. Phys. **53**, 970 (1975).
- [33] H. R. Krishna-murthy, J. W. Wilkins, and K. G. Wilson, Phys. Rev. B **21**, 1003 (1980).
- [34] H. R. Krishna-murthy, J. W. Wilkins, and K. G. Wilson, Phys. Rev. B **21**, 1044 (1980).
- [35] N. L. Dickens and D. E. Logan, J. Phys.: Condens. Matter **13**, 4505 (2001).
- [36] E. Dagotto, Rev. Mod. Phys. **66**, 763 (1994).
- [37] M. Caffarel and W. Krauth, Phys. Rev. Lett. **72**, 1545 (1994).
- [38] Q. Si, M. J. Rozenberg, G. Kotliar, and A. E. Ruckenstein, Phys. Rev. Lett. **72**, 2761 (1994).
- [39] G. Kotliar and A. E. Ruckenstein, Phys. Rev. Lett. **57**, 1362 (1986).
- [40] N. E. Bickers, Rev. Mod. Phys. **59**, 845 (1987).
- [41] J. Hubbard, Proc. R. Soc. Lond. A **277**, 237 (1964).
- [42] J. C. Chen, A. M. Chang, and M. R. Melloch, Phys. Rev. Lett. **92**, 176801 (2004).
- [43] O. Sakai, Y. Shimizu, and T. Kasuya, Solid State Commun. **75**, 81 (1990).
- [44] I. Affleck, A. W. W. Ludwig, and B. A. Jones, Phys. Rev. B **52**, 9528 (1995).

Supplemental Materials for

Hierarchical Liouville-space approach for accurate and universal characterization of quantum impurity systems

ZhenHua Li,¹ NingHua Tong,¹ Xiao Zheng,^{2,*} Dong Hou,²
JianHua Wei,^{1,†} Jie Hu,^{3,4} and YiJing Yan^{2,3,‡}

¹*Department of Physics, Renmin University of China, Beijing 100872, China*

²*Hefei National Laboratory for Physical Sciences at the Microscale,
University of Science and Technology of China, Hefei, Anhui 230026, China*

³*Department of Chemistry, Hong Kong University of Science and Technology, Hong Kong, China*

⁴*Department of Physics, Capital Normal University, Beijing 100048, China*

(Dated: November 12, 2021)

Contents

I. General remarks on the HEOM formalism	3
A. Accuracy and efficiency of the HEOM approach	3
B. A universal quantum mechanical method for open systems	5
1. The Schrödinger picture versus the Heisenberg picture	5
2. The interaction picture and the Dyson equation	7
C. Linear response theory via the HEOM dynamics	8
D. Evaluation of dynamical observables of quantum impurity systems	10
II. Numerical aspects of the HEOM formalism	11
III. Remarks on application of HEOM approach to strongly correlated quantum impurity systems	14
A. Application to single-impurity Anderson model	14
1. Spectral function of SIAM	14
2. Differential conductance and Kondo temperature	14
3. Spectral tail for Kondo resonance	16
B. Application to two-impurity Anderson model	16
C. Application to multi-impurity Anderson models	17
IV. Comparison between HEOM and other methods for quantum impurity systems	18
A. Comparison with numerical renormalization group method	18
B. Comparison with continuous time quantum Monte Carlo method	19

C. Comparison with refined Green's function equation of motion method	20
D. Comparison with exact diagonalization method	21
E. Comparison with slave-boson mean field theory and non-crossing approximation	22
References	23

I. GENERAL REMARKS ON THE HEOM FORMALISM

The hierarchical equations of motion (HEOM) formalism is established based on the Feynman-Vernon influence functional path-integral theory,¹⁻⁴ and implemented with the Grassmann algebra for fermionic dissipations.^{2,5} Thus, it is formally exact for a general open system coupled to reservoirs bath which satisfies Grassmann Gaussian statistics. The mathematical construction of HEOM has been discussed comprehensively in Refs. 3–6. We shall not repeat the tedious derivations, but just address some key features of the HEOM formalism, particularly for those pertinent to the quantum impurity systems studied in the main text of this work. By elucidating these basic features we will discuss the reasons why the HEOM formalism is not just a formally exact theory, but also leads to an accurate, efficient and universal approach for characterization of quantum impurity systems at finite temperatures.

A. Accuracy and efficiency of the HEOM approach

The efficiency of the HEOM approach is rooted mainly at its nonperturbative nature, as discussed later. As a result, it converges often at a relatively low tier level ($L \lesssim 4$). This appealing feature is related to the fact that the HEOM formalism is of finite support, as seen below.

(i) The HEOM formalism is of finite support by a maximum tier level L_{\max} , although numerically it is usually too high to reach. Let us start with the HEOM, Eq. (1) of main text, in which the basic variables are a set of ADOs, $\{\rho_{j_1 \dots j_n}^{(n)}(t); n = 0, 1, \dots, L\}$, with L denoting the converged or truncated tier level in practice. The reduced system density operator is set to be the zeroth-order ADO; *i.e.*, $\rho^{(0)}(t) \equiv \rho(t) = \text{tr}_{\text{res}}[\rho_{\text{total}}(t)]$, with tr_{res} representing the trace over all reservoir environment degrees of freedom. In constructing HEOM, the influence of reservoirs enters via the reservoir correlation functions $\{C_{\mu\nu}^{\pm}(t)\}$, which are related to the inverse Laplace-Fourier transform of the self-energy functions via $C_{\mu\nu}^{+}(t) = i[\Sigma_{\mu\nu}^{<}(t)]^*$ and $C_{\mu\nu}^{-}(t) = i\Sigma_{\mu\nu}^{>}(t)$. To achieve formally close HEOM, $\{C_{\mu\nu}^{\pm}(t)\}$ are expanded in exponential series. Without loss of generality, consider $C_{\mu\nu}^{\sigma}(t) = \delta_{\mu\nu} \sum_{m=1}^M \eta_{\mu m}^{\sigma} e^{-\gamma_{\mu m}^{\sigma} t}$, with the total number of distinct exponential terms being $K = 2MN_{\mu}$, where the factor 2 comes from the choice of $\sigma = +$ or $-$, M is determined by resolution of reservoir memory, and N_{μ} denotes the number of system states through which the itinerant electrons transferring into ($\sigma = +$) and out of ($\sigma = -$) the central system. In writing the HEOM (1) and the involving ADOs, we adopt the abbreviation $j \equiv (\sigma\mu m)$, so that $\gamma_j \equiv \gamma_{\mu m}^{\sigma}$. Thus, the damping term in Eq. (1) collects all involving exponents. Denote also $\bar{j} \equiv (\bar{\sigma}\mu m)$, with $\bar{\sigma}$ being the opposite sign of σ . Involved are also the superoperators, $\mathcal{A}_{\bar{j}} \equiv \mathcal{A}_{\mu}^{\bar{\sigma}}$ and $\mathcal{C}_j \equiv \mathcal{C}_{\mu m}^{\sigma}$, defined via their actions on an arbitrary operator of fermionic or bosonic nature, \hat{O}^{F} or \hat{O}^{B} , respectively, by

$$\mathcal{A}_{\mu}^{\sigma} \hat{O}^{\text{F}} \equiv [\hat{a}_{\mu}^{\sigma}, \hat{O}^{\text{F}}] \quad \text{and} \quad \mathcal{C}_{\mu m}^{\sigma} \hat{O}^{\text{F}} \equiv \eta_{\mu m}^{\sigma} \hat{a}_{\mu}^{\sigma} \hat{O}^{\text{F}} + (\eta_{\mu m}^{\bar{\sigma}})^* \hat{O}^{\text{F}} \hat{a}_{\mu}^{\sigma}, \quad (\text{S1a})$$

or

$$\mathcal{A}_\mu^\sigma \hat{O}^B \equiv \{\hat{a}_\mu^\sigma, \hat{O}^B\} \quad \text{and} \quad \mathcal{C}_{\mu m}^\sigma \hat{O}^B \equiv \eta_{\mu m}^\sigma \hat{a}_\mu^\sigma \hat{O}^B - (\eta_{\mu m}^\sigma)^* \hat{O}^B \hat{a}_\mu^\sigma. \quad (\text{S1b})$$

In particular, while the reduced system density operator $\rho \equiv \rho^{(0)}$ and its associated even-tier ADOs $\{\rho^{(2k)}\}$ are bosonic, the odd-tier $\{\rho^{(2k+1)}\}$ are fermionic.

Moreover, the subscription index set $(j_1 \cdots j_n)$ in a generic n^{th} -tier ADO $\rho_{j_1 \cdots j_n}^{(n)}$ belongs to an ordered set of n *distinct* j -indices. Swapping any two of them leads to a minus sign to the ADO, *i.e.*, $\rho_{j_r j_p} = -\rho_{j_p j_r}$. As a result, the number K of distinct j -indices is equal to not only the number of the first-tier ADOs in total, but also the maximum hierarchical level ($L_{\text{max}} = K$) as by the full HEOM theory. Apparently, the number of the n^{th} -tier ADOs is $\frac{K!}{n!(K-n)!}$, while the total number of unknowns to solve, up to the truncated tier level L , is $\sum_{n=0}^L \frac{K!}{n!(K-n)!} \leq 2^K$, as $L \leq K$. The overall computational cost increases dramatically with both L and K .

To minimize the computational expenditure while maintaining the quantitative accuracy, various reservoir spectrum decomposition schemes (in relation to the K size) have been developed, including the Matsubara spectrum decomposition,⁵ the hybrid Matsubara decomposition-frequency dispersion scheme,⁶ the partial fractional decomposition,⁷ and the recently proposed Padé spectrum decomposition (PSD) scheme.^{8,9} Among all these schemes, the PSD scheme provides an optimal basis to exploit the different characteristic time scales associated with system-reservoir dissipation processes, and hence has the best performance. It leads to an optimal construction of HEOM, with the minimal size of K .

(*ii*) The HEOM formalism is nonperturbative. An important feature of the formalism is that for noninteracting electronic systems (*e.g.* the single-impurity Anderson model (SIAM) with $U = 0$) that are characterized completely by single-particle properties, the resultant HEOM terminate automatically at second tier level ($L = 2$) without approximation.⁵ This feature highlights the nonperturbative nature of the HEOM approach. The underlying hierarchy construction resolves nonperturbatively the combined effects of e - e interaction, system-reservoir dissipative couplings, and non-Markovian memory of reservoir. For quantum impurity systems with nonzero e - e interactions (*e.g.* the SIAM with $U \neq 0$), in principle the hierarchy extends to the K -tier level, as $L_{\text{max}} = K$ discussed earlier. In practice, the calculation results usually converge quantitatively at a low truncation tier ($L \leq 4$), for weak to medium system-reservoir coupling strength. It is important to verify the numerical convergence with the increasing L , and such testing procedure has been carried out for all calculations presented in the main text and also in the Supplemental Materials.

The above features imply the following analogies of the HEOM formalism to conventional many-particle quantum mechanics theories. The full HEOM theory (with $L_{\text{max}} = K$) having a total of 2^K unknowns resembles the K -particle full-space configuration interaction theory, but now for K dissipatons resulted from decomposition of reservoir correlation functions. On the other hand, practically the HEOM formalism resembles a certain coupled-cluster method, as it converges rapidly at a relatively low truncation tier level.

B. A universal quantum mechanical method for open systems

The versatility of the HEOM formalism is rooted at the fact that reduced system dynamics is completely representable in a linear space, referred as the HEOM space hereafter. Such a linear space can be deemed as an extension of conventional Liouville space to open systems. In this subsection, we will establish the HEOM space and elaborate its associated algebra. We will demonstrate that the HEOM space is naturally compatible with the Schrödinger picture, the Heisenberg picture, and the interaction picture of the HEOM formalism. Linear response theory can be established in the HEOM space for open quantum systems. Its application to the evaluation of system correlation functions and response functions will be presented in Sec. IC. In particular, the calculation of various dynamical properties of quantum impurity systems, such as the spectral function, dynamic admittance, and local magnetic susceptibility, will be discussed in Sec. ID.

1. The Schrödinger picture versus the Heisenberg picture

Let us start with the Schrödinger/Heisenberg picture in the conventional Liouville (or Hilbert) space of isolated systems. Consider the expectation value of a system dynamical variable,

$$\bar{A}(t) = \text{tr}[\hat{A}\rho(t)] \equiv \langle\langle\hat{A}|\rho(t)\rangle\rangle = \langle\langle\hat{A}(t)|\rho(0)\rangle\rangle. \quad (\text{S2})$$

The last two quantities are the evaluations in the Schrödinger picture and the Heisenberg picture, respectively. The former is described by the Liouville-von Neumann equation, $\dot{\rho} = -i\mathcal{L}\rho = -i[H_s, \rho]$, for isolated systems with $\rho(t) = \mathcal{G}(t, \tau)\rho(\tau)$. The Heisenberg picture is usually defined only for time-independent system Hamiltonian H_s cases. The corresponding Liouville-space propagator of the isolated system is of the translational invariance in time and given by $\mathcal{G}(t, \tau) = \mathcal{G}(t - \tau) = e^{-i\mathcal{L}(t - \tau)}$. The Heisenberg picture is then $\hat{A}(t) = \hat{A}\mathcal{G}(t)$ or equivalently $\frac{\partial}{\partial t}\hat{A} = -i\hat{A}\mathcal{L} = -i[\hat{A}, H]$ in isolated systems.

To identify the HEOM space and the corresponding Heisenberg picture, we recast Eq. (S2) with its HEOM-space evaluation,

$$\bar{A}(t) = \langle\langle\hat{\mathbf{A}}(0)|\boldsymbol{\rho}(t)\rangle\rangle = \langle\langle\hat{\mathbf{A}}(t)|\boldsymbol{\rho}(0)\rangle\rangle. \quad (\text{S3})$$

The above identities go by

$$\boldsymbol{\rho}(t) \equiv \left\{ \rho_{j_1 \dots j_n}^{(n)}(t); n = 0, 1, \dots, L \right\}, \quad (\text{S4})$$

and

$$\hat{\mathbf{A}}(t) \equiv \left\{ \hat{A}_{j_n \dots j_1}^{(n)}(t); n = 0, 1, \dots, L \right\}, \quad (\text{S5})$$

with the (by-definition) initial conditions of $\hat{A}^{(0)}(t = 0) \equiv \hat{A}$ and $\hat{A}_{j_n \dots j_1}^{(n > 0)}(t = 0) \equiv 0$. The

HEOM-space inner product is defined by

$$\langle\langle \mathbf{A} | \mathbf{B} \rangle\rangle \equiv \sum_{n=0}^L \sum_{j_1 \cdots j_n} \langle\langle A_{j_n \cdots j_1}^{(n)} | B_{j_1 \cdots j_n}^{(n)} \rangle\rangle. \quad (\text{S6})$$

The $\langle\langle \cdot | \cdot \rangle\rangle$ on the right-hand-side (rhs) has been given by the second identity of Eq. (S2). The bra $\langle\langle \mathbf{A} |$ has the involving operators in a row vector, while the ket $|\mathbf{B}\rangle\rangle$ a column vector. Consequently, the j -indexes set $(j_n \cdots j_1)$ in the former is of the reversed order from the $(j_1 \cdots j_n)$ in the latter.

Let us write the Schrödinger picture of the HEOM formalism as

$$\dot{\boldsymbol{\rho}}(t) = -i\mathcal{L}\boldsymbol{\rho}(t). \quad (\text{S7})$$

It is just the matrix form of HEOM (1); i.e.,

$$\begin{aligned} \frac{\partial}{\partial t} \rho_{j_1 \cdots j_n}^{(n)} = & -i \left(\mathcal{L} - i \sum_{r=1}^n \gamma_{j_r} \right) \rho_{j_1 \cdots j_n}^{(n)} - i \sum_j \mathcal{A}_{\bar{j}} \rho_{j_1 \cdots j_n j}^{(n+1)} \\ & - i \sum_{r=1}^n (-)^{n-r} \mathcal{C}_{j_r} \rho_{j_1 \cdots j_{r-1} j_{r+1} \cdots j_n}^{(n-1)}. \end{aligned} \quad (\text{S8})$$

The HEOM-space generator \mathcal{L} is a matrix of superoperators defined by Eq. (S8). It dictates the HEOM-space propagator $\mathcal{G}(t) = e^{-i\mathcal{L}t}$, for both $\boldsymbol{\rho}(t) = \mathcal{G}(t)\boldsymbol{\rho}(0)$ and $\hat{\mathbf{A}}(t) = \hat{\mathbf{A}}(0)\mathcal{G}(t)$. The HEOM in the Heisenberg picture assumes therefore

$$\frac{\partial}{\partial t} \hat{\mathbf{A}} = -i\hat{\mathbf{A}}\mathcal{L}, \quad (\text{S9})$$

with the row vector $\hat{\mathbf{A}}$ defined in Eq. (S5).

To have the explicit Heisenberg HEOM expression, consider the matrix form of Eq. (S8), with the part involving $\rho_{j_1 \cdots j_n}^{(n)}$ explicitly being highlighted as (denoting $\mathcal{L}_{\mathbf{j}_n} \equiv \mathcal{L} - i \sum_{r=1}^n \gamma_{j_r}$)

$$\frac{\partial}{\partial t} \begin{bmatrix} \times \\ \rho_{j_1 \cdots j_{r-1} j_{r+1} \cdots j_n}^{(n-1)} \\ \rho_{j_1 \cdots j_n}^{(n)} \\ \rho_{j_1 \cdots j_n j}^{(n+1)} \\ \times \end{bmatrix} = -i \begin{bmatrix} \times & \times & 0 & 0 & 0 \\ \times & \times & (-)^{n-r} \mathcal{A}_{\bar{j}_r} & 0 & 0 \\ 0 & (-)^{n-r} \mathcal{C}_{j_r} & \mathcal{L}_{\mathbf{j}_n} & \mathcal{A}_{\bar{j}} & 0 \\ 0 & 0 & \mathcal{C}_j & \times & \times \\ 0 & 0 & 0 & \times & \times \end{bmatrix} \begin{bmatrix} \times \\ \rho_{j_1 \cdots j_{r-1} j_{r+1} \cdots j_n}^{(n-1)} \\ \rho_{j_1 \cdots j_n}^{(n)} \\ \rho_{j_1 \cdots j_n j}^{(n+1)} \\ \times \end{bmatrix}.$$

In writing the second row of the above equation for $\rho_{j_1 \cdots j_{r-1} j_{r+1} \cdots j_n}^{(n-1)}$, we exploit the identity of $\rho_{j_1 \cdots j_{r-1} j_{r+1} \cdots j_n j_r}^{(n)} = (-)^{n-r} \rho_{j_1 \cdots j_n}^{(n)}$. The Heisenberg counterpart is therefore of

$$\frac{\partial}{\partial t} \begin{bmatrix} \times \\ \hat{A}_{j_n \cdots j_{r+1} j_{r-1} \cdots j_1}^{(n-1)} \\ \hat{A}_{j_n \cdots j_1}^{(n)} \\ \hat{A}_{j j_n \cdots j_1}^{(n+1)} \\ \times \end{bmatrix}^T = -i \begin{bmatrix} \times \\ \hat{A}_{j_n \cdots j_{r+1} j_{r-1} \cdots j_1}^{(n-1)} \\ \hat{A}_{j_n \cdots j_1}^{(n)} \\ \hat{A}_{j j_n \cdots j_1}^{(n+1)} \\ \times \end{bmatrix}^T \begin{bmatrix} \times & \times & 0 & 0 & 0 \\ \times & \times & (-)^{n-r} \mathcal{A}_{\bar{j}_r} & 0 & 0 \\ 0 & (-)^{n-r} \mathcal{C}_{j_r} & \mathcal{L}_{\mathbf{j}_n} & \mathcal{A}_{\bar{j}} & 0 \\ 0 & 0 & \mathcal{C}_j & \times & \times \\ 0 & 0 & 0 & \times & \times \end{bmatrix}.$$

It reads explicitly as

$$\begin{aligned} \frac{\partial}{\partial t} \hat{A}_{j_n \dots j_1}^{(n)} &= -i \hat{A}_{j_n \dots j_1}^{(n)} \left(\mathcal{L} - i \sum_{r=1}^n \gamma_{j_r} \right) - i \sum_j \hat{A}_{j j_n \dots j_1}^{(n+1)} \mathcal{C}_j \\ &\quad - i \sum_{r=1}^n (-)^{n-r} \hat{A}_{j_n \dots j_{r+1} j_{r-1} \dots j_1}^{(n-1)} \mathcal{A}_{j_r}. \end{aligned} \quad (\text{S10})$$

This is the Heisenberg counterpart of Eq. (S8). The Grassmann-parity associated superoperators \mathcal{A}_j and \mathcal{C}_j act now from the right or backward side on the specified operators that are of either fermionic or bosonic in nature, dictated by that of $\hat{A}^{(0)} \equiv \hat{A}$ and then alternates in every subsequent tier. We have the following equivalence to Eq. (S1):

$$\hat{O}^F \mathcal{A}_\mu^\sigma \equiv [\hat{O}^F, \hat{a}_\mu^\sigma] \quad \text{and} \quad \hat{O}^F \mathcal{C}_{\mu m}^\sigma \equiv \eta_{\mu m}^\sigma \hat{O}^F \hat{a}_\mu^\sigma + (\eta_{\mu m}^\sigma)^* \hat{a}_\mu^\sigma \hat{O}^F, \quad (\text{S11a})$$

or

$$\hat{O}^B \mathcal{A}_\mu^\sigma \equiv \{\hat{O}^B, \hat{a}_\mu^\sigma\} \quad \text{and} \quad \hat{O}^B \mathcal{C}_{\mu m}^\sigma \equiv \eta_{\mu m}^\sigma \hat{O}^B \hat{a}_\mu^\sigma - \hat{O}^B \hat{a}_\mu^\sigma (\eta_{\mu m}^\sigma)^*. \quad (\text{S11b})$$

2. The interaction picture and the Dyson equation

The HEOM space interaction picture can also be readily established straightforwardly from its Hilbert-space counterpart. Let us revisit Eq. (S8), with $\mathcal{L} + \delta\mathcal{L}_{\text{pr}}(t)$ and thus the HEOM generator $\mathcal{L} + \delta\mathcal{L}_{\text{pr}}(t)$. Here, \mathcal{L} is the impurities system Liouvillian that may be time-dependent, for example, in the presence of external pump fields. On the other hand, $\delta\mathcal{L}_{\text{pr}}(t)$ denotes the additional contribution from the external “probe” field interrogation on the system. Let $\mathcal{G}_{\text{pr}}(t, \tau)$ be the total HEOM propagator in the presence of the probe field, while $\mathcal{G}(t, \tau)$ be the probe-free counterpart; i.e., $\frac{\partial}{\partial t} \mathcal{G}_{\text{pr}}(t, \tau) = -i(\mathcal{L} + \delta\mathcal{L}_{\text{pr}}) \mathcal{G}_{\text{pr}}(t, \tau)$ and $\frac{\partial}{\partial t} \mathcal{G}(t, \tau) = -i\mathcal{L} \mathcal{G}(t, \tau)$, respectively. The standard interaction picture technique leads then readily to the Dyson’s equation with the HEOM dynamics the form of

$$\mathcal{G}_{\text{pr}}(t, \tau) = \mathcal{G}(t, \tau) - i \int_{\tau}^t d\tau' \mathcal{G}_{\text{pr}}(t, \tau') \delta\mathcal{L}_{\text{pr}}(\tau') \mathcal{G}(\tau', \tau), \quad (\text{S12})$$

where τ denotes *any time before* the specified probe field interrogation. In terms of the interrogated $\boldsymbol{\rho}(t) + \delta\boldsymbol{\rho}(t)$, or $\delta\boldsymbol{\rho}(t) = [\mathcal{G}_{\text{pr}}(t, \tau) - \mathcal{G}(t, \tau)] \boldsymbol{\rho}(\tau)$, the above Dyson equation can be recast as (setting $\tau \rightarrow -\infty$)

$$\delta\boldsymbol{\rho}(t) = -i \int_{-\infty}^t d\tau' \mathcal{G}_{\text{pr}}(t, \tau') \delta\mathcal{L}_{\text{pr}}(\tau') \boldsymbol{\rho}(\tau') = -i \int_{-\infty}^t d\tau' \mathcal{G}_{\text{pr}}(t, \tau') [\delta\mathcal{L}_{\text{pr}}(\tau') \boldsymbol{\rho}(\tau')]. \quad (\text{S13})$$

In writing the second identity, we emphasize the fact that $\delta\mathcal{L}_{\text{pr}}(t)$ appears in only but every diagonal matrix element of the HEOM space generator, so that $\delta\mathcal{L}_{\text{pr}}(t) = \delta\mathcal{L}_{\text{pr}}(t) \mathcal{I}$, where \mathcal{I} is the unit matrix. Hence, $\delta\mathcal{L}_{\text{pr}}(t) \boldsymbol{\rho}(t) = \{\delta\mathcal{L}_{\text{pr}}(t) \rho_{j_1 \dots j_n}^{(n)}(t); n = 0, \dots, L\} = \delta\mathcal{L}_{\text{pr}}(t) \boldsymbol{\rho}(t)$, as inferred from Eq. (S4).

C. Linear response theory via the HEOM dynamics

Consider now the equilibrium HEOM dynamics where the impurities system is initially at thermal equilibrium, $\boldsymbol{\rho}(t_0) = \boldsymbol{\rho}^{\text{eq}}(T)$ at a given temperature T , and there is no time-dependent pump field. Therefore, the probe-free propagator is of the translational invariance in time, $\mathcal{G}(t, \tau) = \mathcal{G}(t - \tau)$, and further that $\boldsymbol{\rho}(\tau') = \mathcal{G}(\tau' - t_0)\boldsymbol{\rho}(t_0) = \boldsymbol{\rho}^{\text{eq}}(T)$ in the integrand of Eq.(S13). Together with the Dyson equation, Eq.(S13) for the equilibrium dynamics reads

$$\delta\boldsymbol{\rho}(t) = \sum_{n=1}^{\infty} (-i)^n \int_{-\infty}^t d\tau_n \cdots \int_{-\infty}^{\tau_2} d\tau_1 \mathcal{G}(t - \tau_n) \delta\mathcal{L}_{\text{pr}}(\tau_n) \mathcal{G}(\tau_n - \tau_{n-1}) \cdots \delta\mathcal{L}_{\text{pr}}(\tau_1) \boldsymbol{\rho}^{\text{eq}}(T). \quad (\text{S14})$$

This resembles the celebrated Hilbert-space time-dependent perturbation theory via interaction picture. Note that the thermal equilibrium $\boldsymbol{\rho}^{\text{eq}}(T) \equiv \{\rho_{j_1 \cdots j_n}^{(n); \text{eq}}(T); n = 0, \cdots, L\}$ is a steady-state solution of the HEOM (S8), in the absence of time-dependent external fields; see its evaluation in Sec. II. The resulting nonzero ADOs, $\rho_{j_1 \cdots j_n}^{(n>0); \text{eq}}(T) \neq 0$, reflect the initial system-reservoirs correlations.

The above observations highlight a straightforward equivalence mapping between the conventional Hilbert space and the HEOM space formulations for the evaluations of various correlation and response functions of impurity systems. Consider, for example, the steady-state two-time correlation function between two arbitrary dynamical variables \hat{A} and \hat{B} of the impurity system of interest. We have [*cf.* Eqs. (S2) and (S3)]

$$\tilde{C}_{AB}(t) = \langle \hat{A}(t) \hat{B}(0) \rangle = \langle \langle \hat{A}(t) | \hat{B} \rho_{\text{total}}^{\text{eq}}(T) \rangle \rangle = \langle \langle \hat{A}(t) | \hat{B} \boldsymbol{\rho}^{\text{eq}}(T) \rangle \rangle. \quad (\text{S15})$$

Similarly, the response function will be

$$\chi_{AB}(t) = i \langle [\hat{A}(t), \hat{B}(0)] \rangle = i \langle \langle \hat{A}(t) | [\hat{B}, \rho_{\text{total}}^{\text{eq}}(T)] \rangle \rangle = i \langle \langle \hat{A}(t) | [\hat{B}, \boldsymbol{\rho}^{\text{eq}}(T)] \rangle \rangle. \quad (\text{S16})$$

The proof will be exemplified with the response function of Eq. (S16) as follows.

Application of Eq. (S14) is to be illustrated with the HEOM evaluation of correlation and response functions of impurity systems via the linear response theory (LRT) which applies to the HEOM linear space defined in Sec. IB.

Regarding the LRT, we are primarily interested in how system properties (such as the expectation value of a system observable \hat{A}) respond to an external perturbation in the physical subspace of the system. Suppose the perturbation Hamiltonian assumes the following form

$$H_{\text{pr}}(t) = -\hat{B} \epsilon_{\text{pr}}(t), \quad (\text{S17})$$

where \hat{B} is a Hermitian system operator, and $\epsilon_{\text{pr}}(t)$ is the time-dependent perturbative field which takes effect from t_0 [$\epsilon_{\text{pr}}(t < t_0) = 0$]. The induced change in the expectation value of a system observable \hat{A} due to the presence of $H_{\text{pr}}(t)$ is

$$\delta\hat{A}(t) = \text{tr}_{\text{s}}[\hat{A} \delta\boldsymbol{\rho}(t)] = \langle \langle \hat{A} | \delta\boldsymbol{\rho}(t) \rangle \rangle. \quad (\text{S18})$$

By using the first order perturbation in Eq. (S14), we arrive at

$$\delta\rho(t) = -i \int_0^t d\tau \mathcal{G}(t-\tau) \delta\mathcal{L}_{\text{pr}}(\tau) \rho^{\text{eq}}(T). \quad (\text{S19})$$

To proceed, we define the time-independent HEOM-space superoperator $\hat{\mathcal{B}}$ as

$$\hat{\mathcal{B}} \equiv -\delta\mathcal{L}_{\text{pr}}(t)/\epsilon_{\text{pr}}(t), \quad (\text{S20})$$

whose action can be determined as

$$\hat{\mathcal{B}}\rho = [\hat{B}, \rho]. \quad (\text{S21})$$

Inserting Eq. (S21) into (S19), we finally get

$$\delta\hat{A}(t) = i \int_0^t d\tau \langle\langle \hat{A}(0) | \mathcal{G}(t-\tau) \hat{\mathcal{B}} | \rho^{\text{eq}}(T) \rangle\rangle \epsilon_{\text{pr}}(\tau), \quad (\text{S22})$$

from which we are ready to define the response function in HEOM space as

$$\chi_{AB}(t, \tau) \equiv i \langle\langle \hat{A}(0) | \mathcal{G}(t-\tau) \hat{\mathcal{B}} | \rho^{\text{eq}}(T) \rangle\rangle. \quad (\text{S23})$$

The correlation function in HEOM space can be similarly defined as

$$\tilde{C}_{AB}(t, \tau) \equiv \langle\langle \hat{A}(0) | \mathcal{G}(t-\tau) \hat{B} | \rho^{\text{eq}}(T) \rangle\rangle, \quad (\text{S24})$$

where $\hat{B}\rho^{\text{eq}}(T) = \{\hat{B}\rho^{(n);\text{eq}}; n = 0, 1, \dots, L\}$. By setting $\tau = 0$ while noting $\hat{A}(t) = \hat{A}(0)\mathcal{G}(t)$, Eqs. (S23) and (S24) recover Eqs. (S16) and (S15) immediately.

The dynamical observables of our primary interest in the present work are the system correlation function and spectral function, which associate with each other through the fluctuation-dissipation theorem (FDT) at thermal equilibrium. Consider, for example, the retarded and advanced single-particle Green's functions in terms of the correlation functions,

$$G_{AB}^r(t) = -i\theta(t) \langle\{ \hat{A}(t), \hat{B} \}\rangle = -i\theta(t) [\tilde{C}_{AB}(t) + \tilde{C}_{BA}(-t)], \quad (\text{S25})$$

and

$$G_{AB}^a(t) = i\theta(-t) \langle\{ \hat{A}(t), \hat{B} \}\rangle = i\theta(-t) [\tilde{C}_{AB}(t) + \tilde{C}_{BA}(-t)]. \quad (\text{S26})$$

Here, the Green's functions in our theory is defined for two arbitrary operators \hat{A} and \hat{B} . We now focus on cases where $\hat{A} = \hat{B}^\dagger$ (e.g., $\hat{A} = a$ and $\hat{B} = a^\dagger$ for conventional fermionic Green's functions). In such circumstances, $\tilde{C}_{AB}^*(t) = \tilde{C}_{AB}(-t)$ follows by definition. Using this relation in the Fourier transform of Eqs. (S25)–(S26) leads to $G_{AB}^a(\omega) = [G_{AB}^r(\omega)]^*$. We can further define the spectral function $J_{AB}(\omega)$ as

$$J_{AB}(\omega) \equiv -\frac{1}{\pi} \text{Im} [G_{AB}^r(\omega)] = -\frac{1}{2\pi i} [G_{AB}^r(\omega) - G_{AB}^a(\omega)]. \quad (\text{S27})$$

Let $C_{AB}(\omega) \equiv \frac{1}{2} \int_{-\infty}^{\infty} dt e^{i\omega t} \tilde{C}_{AB}(t)$, which satisfies $C_{BA}(-\omega) = e^{-\beta\omega} C_{AB}(\omega)$, the detailed-balance relation at thermal equilibrium. By combining Eqs. (S25)–(S27), we arrive at the FDT of

$$J_{AB}(\omega) = \frac{1}{\pi} (1 + e^{-\beta\omega}) C_{AB}(\omega). \quad (\text{S28})$$

D. Evaluation of dynamical observables of quantum impurity systems

In principle, the dynamical correlation of any two system operators (\hat{A} and \hat{B}) can be calculated by using the HEOM-space LRT via Eq. (S24). This allows us to evaluate at quantitative accuracy a variety of dynamical observables of experimental significance, such as the Green's functions and spectral function of the system, local electric and magnetic susceptibilities, and dynamic admittance (inverse of complex impedance), *etc.* The calculation of system Green's functions and spectral function will be presented in Sec. II. Here, we take the local magnetic susceptibility as an example to illustrate how the response properties are evaluated by using the HEOM approach.

The local magnetic susceptibility χ^m describes the magnetization of an impurity in linear-order response to an external magnetic field applied locally at the impurity site. For simplicity, we consider the case that the magnetic field is applied only along the z -direction, so is the induced spin polarization for electrons on the impurity.

$$M_z(\omega) = \chi^m(\omega) H_z(\omega). \quad (\text{S29})$$

Here, $M_z(\omega)$, $H_z(\omega)$, and $\chi^m(\omega)$ are the local magnetization, local magnetic field, and local magnetic susceptibility of frequency ω along z -direction, respectively. Note that $M_z(\omega) = \mathcal{F}[\langle \hat{m}_z(t) \rangle]$, with the local magnetization operator being

$$\hat{m}_z = g\mu_B \hat{S}_z = \frac{1}{2}g\mu_B \sum_i \left(a_{i\uparrow}^\dagger a_{i\uparrow} - a_{i\downarrow}^\dagger a_{i\downarrow} \right). \quad (\text{S30})$$

Here, g is the gyromagnetic ratio, μ_B the Bohr magnetization, and \hat{S}_z is the electron spin polarization operator along z -direction for the impurity.

Upon application of an *ac* local magnetic field, $H_z(t)$, the system perturbation Hamiltonian is

$$\hat{H}_{\text{pr}}(t) = -\hat{m}_z H_z(t). \quad (\text{S31})$$

Apparently, Eq. (S31) assumes the same form as Eq. (S17), with \hat{m}_z playing the role of \hat{B} . The physical observable of primary interest is $\hat{A} = \hat{m}_z$. Based on the HEOM-space LRT, the local magnetic susceptibility is expressed as

$$\tilde{\chi}^m(t) = i\langle [\hat{m}_z(t), \hat{m}_z] \rangle = i\langle \langle \hat{\mathbf{m}}_z(0) | \mathcal{G}(t) | [\hat{m}_z, \boldsymbol{\rho}^{\text{eq}}] \rangle \rangle. \quad (\text{S32})$$

Equation (S32) is formally analogous to Eq. (S23), and hence $\tilde{\chi}^m(t)$ can be readily calculated by solving the quantum Liouville propagator $\mathcal{G}(t)$ in HEOM space. The *dynamic* (frequency-dependent) local magnetic susceptibility is then obtained via Fourier transform, *i.e.*, $\chi^m(\omega) = \mathcal{F}[\tilde{\chi}^m(t)]$. In particular, the *static* local magnetic susceptibility is just its zero-frequency component, $\chi^m(\omega = 0)$. The above formulas can be easily extended to scenario of noncollinear spin.

The above procedures are applicable to a variety of dynamical observables, such as the local electric susceptibility. However, the evaluation of dynamic admittance is somewhat different. It involves the calculation of response function, $\tilde{\chi}_{\alpha\alpha'}^G(t) = -i\langle[\hat{I}_\alpha(t), \hat{N}_{\alpha'}]\rangle$, where \hat{I}_α and $\hat{N}_{\alpha'}$ are the current operator for α -reservoir and electron number operator for α' -reservoir, respectively. Although \hat{I}_α and $\hat{N}_{\alpha'}$ are not “system” operators, $\tilde{\chi}_{\alpha\alpha'}^G(t)$ can still be evaluated by making use of the quantum Liouville propagator in HEOM space. The detailed formulation and numerical demonstrations will be published elsewhere.

It is important to emphasize that the HEOM approach is capable of addressing the nonequilibrium electronic dynamics under arbitrary time-dependent external fields. This thus provides an alternative way for the evaluation of dynamical observables, *i.e.*, through the real-time evolution of system reduced density matrix $\rho(t)$ and the ADOs. The expectation value of physical observable is then extracted from $\{\rho^{(n)}(t)\}$. For instance, the dynamic local magnetic susceptibility can be obtained via $\chi^m(\omega) = g\mu_B \mathcal{F}[S_z(t)]/\mathcal{F}[H_z(t)]$, where $S_z(t) = \langle\hat{S}_z\rangle = \text{tr}[\hat{S}_z\rho(t)]$ is the spin polarization for electrons on the impurity under the applied magnetic field $H_z(t)$. Another example is the dynamic admittance, which can be evaluated via $\chi_{\alpha\alpha'}^G(\omega) \equiv \mathcal{F}[\tilde{\chi}_{\alpha\alpha'}^G(t)] = \mathcal{F}[I_\alpha(t)]/\mathcal{F}[-eV_{\alpha'}(t)]$, with $I_\alpha(t)$ and $V_{\alpha'}(t)$ being the time-dependent current and voltage for α - and α' -reservoir, respectively. Note that $I_\alpha(t)$ is extracted from first-tier ADOs; see Ref. [10]. In our previous work, we have carried out comprehensive studies on the dynamic admittance of open impurity systems; see Refs. [10,11]. Moreover, such an approach allows us to go beyond the linear regime and explore system properties in far-from-equilibrium situations. Furthermore, the static response ($\omega = 0$) to external perturbation can be obtained straightforwardly by solving stationary states corresponding to fixed external fields. For instance, the differential conductance data (dI/dV) displayed in Fig. 3 of main text are extracted from steady-state current under different bias voltages via a finite-field treatment.

To summarize, there are two ways to evaluate the dynamical observables of quantum impurity systems within the framework of HEOM theory. One is to calculate the relevant correlation/response function via the HEOM-space LRT; while the other is to calculate the nonequilibrium static/dynamic electronic response to applied external fields. These two ways are completely equivalent in the linear response regime.

II. NUMERICAL ASPECTS OF THE HEOM FORMALISM

The numerical implementation of the HEOM method for calculations of dynamical properties of open electronic system, such as transient transport current through quantum dot systems under time-dependent applied voltages, has been addressed in our previous publications; see Refs. [6,10–12]. Our recent improvement on numerical algorithms and codes concerns mainly the follows: (i) improve the numerical efficiency by making use of various advanced numerical techniques, so that the quantum impurity systems in strong correlation

regime can be treated accurately with the presently available computational resources; and (ii) extend the HEOM method to evaluation of dynamical observables at equilibrium state.

To reduce the computational cost, we have employed the Padé spectrum decomposition scheme^{8,9} to construct the HEOM, the quasi-minimal residual (QMR) method^{13,14} to solve the large linear problem for stationary states, and the fourth-order Runge-Kutta¹⁵ or Chebyshev¹⁶ method for the time evolution of quantum Liouville propagator in HEOM space. We have also used sparse matrix algorithms and parallel computing techniques to accelerate the calculations. The detailed descriptions of our numerical code will be published elsewhere. Here, we demonstrate the numerical capability of our HEOM code through the calculations on the same single-impurity Anderson model (SIAM) as studied in Fig. 1 of the main text. Tables S1 and S2 show the computational cost and numerical convergence for the SIAM at relatively high ($T = 1.5 \Delta$) and low ($T = 0.075 \Delta$) temperatures, respectively. In particular, the low temperature brings the SIAM system into the strong correlation (Kondo) regime, and the fourth-tier truncation ($L = 4$) predicts the number of occupied electrons with a minor uncertainty of less than 2×10^{-5} electron.

A variety of system dynamical observables, such as the spectral density function associated with μ th single-electron level of system, $A_\mu(\omega) \equiv J_{\hat{a}_\mu \hat{a}_\mu^\dagger}(\omega)$, can be evaluated in two ways: either with a time-domain scheme or by calculations in the frequency domain.

The time-domain scheme starts with the evaluation of system correlation functions $\tilde{C}_{\hat{a}_\mu^\dagger \hat{a}_\mu}(t)$ and $\tilde{C}_{\hat{a}_\mu \hat{a}_\mu^\dagger}(t)$ through the time evolution of the quantum Liouville propagator $\hat{\mathcal{G}}_{\text{eq}}(t)$ at $t > 0$. The spectral function is then obtained straightforwardly by a half Fourier transform as follows,

$$A_\mu(\omega) = \frac{1}{\pi} \text{Re} \left\{ \int_0^\infty dt \left\{ \tilde{C}_{\hat{a}_\mu^\dagger \hat{a}_\mu}(t) + [\tilde{C}_{\hat{a}_\mu \hat{a}_\mu^\dagger}(t)]^* \right\} e^{i\omega t} \right\}. \quad (\text{S33})$$

The averaged system spectral function is $A(\omega) = \frac{1}{N} \sum_{i=1}^N A_i(\omega)$. However, in practice the time-domain scheme can be very time-consuming, especially for strongly correlated systems at low temperatures, where $A(\omega)$ exhibits prominent Kondo signatures at around zero frequency. In such cases, both $\tilde{C}_{\hat{a}_\mu^\dagger \hat{a}_\mu}(t)$ and $\tilde{C}_{\hat{a}_\mu \hat{a}_\mu^\dagger}(t)$ decay rather slowly at large t , due to the significant long-time reservoir memory component. Consequently, to calculate $A(\omega)$ at low frequency accurately, it is necessary to have the correlation functions propagate to a long enough time.

An alternative scheme is based on the half-Fourier transformed correlation function via

$$\begin{aligned} \bar{C}_{AB}(\omega) &\equiv \int_0^\infty dt C_{AB}(t) e^{i\omega t} = \int_0^\infty dt \langle \langle \mathbf{A} | \hat{\mathcal{G}}_{\text{eq}}(t) | \mathbf{B}_{\text{eq}} \rangle \rangle e^{i\omega t} \\ &= \int_0^\infty dt \langle \langle \mathbf{A} | e^{(i\omega - \hat{\Lambda})t} | \mathbf{B}_{\text{eq}} \rangle \rangle \\ &= -\langle \langle \mathbf{A} | (i\omega - \hat{\Lambda})^{-1} | \mathbf{B}_{\text{eq}} \rangle \rangle = \langle \langle \mathbf{A} | \mathbf{X} \rangle \rangle. \end{aligned} \quad (\text{S34})$$

At a fixed frequency ω , the HEOM-space vector \mathbf{X} is determined by solving the following

linear problem with the QMR algorithm:

$$(i\omega - \hat{\Lambda})\mathbf{X} = -\mathbf{B}_{\text{eq}}. \quad (\text{S35})$$

The system spectral function is then evaluated via

$$A_\mu(\omega) = \frac{1}{\pi} \text{Re} \left[\bar{C}_{\hat{a}_\mu \hat{a}_\mu^\dagger}(\omega) + \bar{C}_{\hat{a}_\mu^\dagger \hat{a}_\mu}(-\omega) \right]. \quad (\text{S36})$$

Within the frequency-domain scheme, $A(\omega)$ is calculated at one frequency point by solving Eqs. (S35) and (S36) once. Therefore, to obtain the whole spectrum of $A(\omega)$, a full scan for the whole frequency domain is needed.

The equivalence between the two schemes is exemplified with Fig. S1, where the spectral function of a SIAM is calculated with both time- and frequency-domain schemes. Apparently, the results out of both schemes agree perfectly with each other, as they should. In practice, a hybrid time- and frequency-domain scheme can be employed. The overall profile of $A(\omega)$ can be obtained with the time-domain scheme, while the detailed structures of the resonance and Kondo peaks which are difficult to resolve by the time-domain algorithm can be exploited with the frequency-domain scheme. This hybrid scheme provides an accurate and efficient method to calculate the full spectrum of $A(\omega)$ for a strongly correlated quantum impurity system in the Kondo regime.

Similarly, the retarded Green's function is evaluated based on system correlation functions with the time- or frequency-domain scheme as follows.

$$G_{\mu\mu}^r(\omega) = -i \int_0^\infty dt \left\{ \tilde{C}_{\hat{a}_\mu \hat{a}_\mu^\dagger}(t) + [\tilde{C}_{\hat{a}_\mu^\dagger \hat{a}_\mu}(t)]^* \right\} e^{i\omega t} = -i \left\{ \bar{C}_{\hat{a}_\mu \hat{a}_\mu^\dagger}(\omega) + [\bar{C}_{\hat{a}_\mu^\dagger \hat{a}_\mu}(-\omega)]^* \right\}. \quad (\text{S37})$$

For an SIAM system, the single-electron retarded Green's function is formally expressed as

$$G_d^r(\omega) = [\omega - \epsilon_d - \Sigma_{\text{res}}^r(\omega) - \Sigma_{\text{ee}}^r(\omega)]^{-1}. \quad (\text{S38})$$

Here, $\Sigma_{\text{res}}^r(\omega)$ is the self-energy due to the dissipative couplings between the impurity and reservoirs. Its imaginary part gives the hybridization function $\Delta(\omega) = -\text{Im}[\Sigma_{\text{res}}^r(\omega)]$, which is calculated from the surface Green's function of the isolated electron reservoirs, or provided as a known property of the reservoirs (such as the Lorentzian lineshape model adopted in this work). $\Sigma_{\text{ee}}^r(\omega)$ is the self-energy due to the presence of electron-electron interaction (the U -term) which reflects the information of electron correlation. With $G_d^r(\omega)$ evaluated by the HEOM approach via Eq. (S37), $\Sigma_{\text{ee}}^r(\omega)$ can be extracted from Eq. (S38) as the only unknown variable.

III. REMARKS ON APPLICATION OF HEOM APPROACH TO STRONGLY CORRELATED QUANTUM IMPURITY SYSTEMS

A. Application to single-impurity Anderson model

1. Spectral function of SIAM

The numerical convergence of HEOM is exemplified via the calculated $A(\omega)$ of an asymmetric SIAM system at different truncation tier L ; see Fig. 1 in the main text, where the resulting $A(\omega)$ converges uniformly to the numerically exact solution with the increasing L . Figure S2 depicts the derivation of $A(\omega)$ calculated at various L from the result obtained at $L_{\max} = 5$. It is observed that the magnitude of difference indeed decreases as L approaches L_{\max} . In particular, there is only rather minor deviation between the calculated $A(\omega)$ at $L = 4$ and that at $L = 5$, which is barely recognizable at around zero frequency.

We also investigate the temperature dependence of $A(\omega)$. Figure S3 plots the calculated $A(\omega)$ of the same asymmetric SIAM system at various temperatures. Apparently, as the temperature increases over an order of magnitude, the two resonance peaks at $\omega = \epsilon_d$ and $\omega = \epsilon_d + U$, which are due to transition between different occupancy states, remain intact. In contrast, the Kondo peak at $\omega = E_F = 0$ almost vanishes at the higher temperature. This clearly highlights the significant role of strong electron correlation in quantum impurity systems.

2. Differential conductance and Kondo temperature

We proceed to examine the zero-bias differential conductance of various two-terminal SIAM systems. This is to verify that the low-temperature physical properties obtained by the HEOM approach indeed follows the correct Kondo scaling relation.

The analytical expression for Kondo temperature of a symmetric SIAM is¹⁷

$$T_K = \sqrt{\frac{U\Delta}{2}} e^{-\pi U/8\Delta + \pi\Delta/2U}. \quad (\text{S39})$$

Equation (S39) is derived based on Bethe Ansatz,¹⁷ and is expected to be valid provided that the relation $\Delta \ll U \ll W$ is satisfied. Here, Δ is the impurity-reservoir coupling strength, and W is the bandwidth of electron reservoirs.

Figure S5 and Figure 3(a) of main text depict the temperature dependence of zero-bias differential conductance (dI/dV) of symmetric SIAM systems with different values of U . Apparently, the dI/dV versus T curves for different values of U display rather scattered distribution; see Fig. S5(a). In contrast, with the temperature scaled by T_K of Eq. (S39), all curves merge into one at $T < T_K$, showing the expected universal Kondo scaling behavior; see Fig. S5(b). Whereas the curves become separated at $T > T_K$, indicating the systems

are outside the Kondo regime. It is important to point out that the second term in the exponent of Eq. (S39) is unnegligible to achieve the universal scaling behavior quantitatively. Moreover, note that as the value of U approaches Δ , T_K of Eq. (S39) is no longer the true Kondo energy scale. This is clearly manifested by the $U = 1.2\Delta$ curve in Fig. S5(b), where the dI/dV versus T/T_K data deviate significantly from the universal scaling curve. Instead, it is found that by taking U as the Kondo energy scale, the universal scaling is retrieved; see the pink squares in Fig. S5(b). It is thus inferred that the Kondo energy scale depends sensitively on the relative magnitudes of relevant parameters (U , Δ , and W). For lower temperatures, a higher truncation level L is necessary to achieve quantitative convergence, which is computationally too demanding for present HEOM approach.

By varying the value of ϵ_d or U while fixing the others, the SIAM is tuned away from the particle-hole symmetry. The degree of asymmetry can be characterized by a parameter $\delta = \epsilon_d + \frac{U}{2}$. It is well known that for an asymmetric SIAM (corresponding to $\delta \neq 0$), its Kondo temperature deviates from the form of Eq. (S39).¹⁸ In particular, it had been derived by Krishna-murthy, Wilkins, and Wilson¹⁹ that the Kondo temperature of an asymmetric SIAM in the local moment regime ($T \ll -\epsilon_d \ll U$ and $\Delta \ll U \ll W$) can be evaluated via

$$\begin{aligned}
\epsilon_d^* &= \epsilon_d - \frac{\Delta}{\pi} \ln \left(\frac{-U}{\epsilon_d^*} \right), \\
\rho_0 J_K &= \frac{2\Delta}{\pi} \left(\frac{1}{|\delta - U/2|} + \frac{1}{|\delta + U/2|} \right), \\
\rho_0 K &= \frac{\Delta}{2\pi} \left(\frac{1}{|\delta - U/2|} - \frac{1}{|\delta + U/2|} \right), \\
\rho_0 \tilde{J}_K &= \rho_0 J_K [1 + (\pi \rho_0 K)^2]^{-1}, \\
T'_K &= 0.182 |\epsilon_d^*| \sqrt{\rho_0 \tilde{J}_K} \exp \left(\frac{-1}{\rho_0 \tilde{J}_K} \right).
\end{aligned} \tag{S40}$$

Here, ϵ_d^* is the renormalized on-site energy. We examine a series of SIAMs in this regime, with fixed ϵ_d but different values of U (and hence different δ). The corresponding dI/dV curves versus T and T/T'_K are depicted in Fig. S6(a) and (b), respectively. The scattered curves in Fig. S6(a) merge into one in Fig. S6(b), indicating that T'_K of Eq. (S40) indeed provides a universal Kondo energy scale for asymmetric SIAM systems. Note that in Fig. S6(b) the $U = 1.6$ meV data (represented by pink triangles) deviate slightly from the universal scaling relation at low temperatures, which is possibly due to the fact that such a value of U approaches to the reservoir bandwidth of $W = 2.0$ meV.

3. Spectral tail for Kondo resonance

It has been predicted that for symmetric SIAM systems, the Kondo peak of scaled spectral function has a slowly varying logarithmic tail as follows,²⁰

$$A(\omega) = \frac{1}{2\pi\Delta} \left\{ \frac{1}{[(4/\pi) \ln(|\omega'|)]^2 + 1} + \frac{5}{[(4/\pi) \ln(|\omega'|)]^2 + 25} \right\}. \quad (\text{S41})$$

Here, $\omega' = \omega/\omega'_m = \omega/[\lambda e^{-\pi U/8\Delta}]$ with $\lambda = \min(W, U/2)$ being the high-energy cut-off. It has been verified that Eq. (S41) fits well with the NRG result at $T = 0$.²⁰

Figure 3(b) of main text plots the spectral function around the Kondo peak calculated by the HEOM approach, which is compared with the analytic curve of Eq. (S41). Clearly, at relatively large scaled frequencies, (say, at $\omega/\omega_k > 150$) the numerical results agree remarkably with the analytic curve under all temperatures studied; while in the low-frequency region, the HEOM results converge consistently to the analytic curve (corresponding to $T = 0$) as the temperature decreases. At even larger frequencies ($\omega/\omega_k > 500$), the Hubbard peak starts to rise, which overwhelms the tail of Kondo resonance peak, and hence this part of $A(\omega)$ does not show up in the comparison.

Figure S7 depicts the comparison between the HEOM calculated $A(\omega)$ for symmetric SIAMs with various values of U and the analytic expression of Eq. (S41). Apparently, the numerical data agree better with the analytic formula as U increases. This is due to the fact that the exponent $e^{-\pi U/8\Delta}$ involved in Eq. (S41) is asymptotically exact in the strong coupling limit.²⁰

The above comparisons clearly affirm that the HEOM approach correctly reproduces the asymptotic logarithmic scaling of Kondo resonance tail.

B. Application to two-impurity Anderson model

As described in the main text, we have applied the HEOM approach to two-impurity Anderson model (TIAM) system. For clarity, a symmetric parallel-coupled two-impurity system is considered. For the TIAM, we focus on how the inter-impurity coupling t affects the system dynamical properties (*e.g.* the spectral function of the impurities) in the presence of strong e - e interaction. Fig. 3 of the main text reveals that with the increasing t , the system exhibits a continuous crossover transition from the Kondo singlet state of individual impurity to the singlet spin-state between the two impurities. This is affirmed by the impressive agreement between the essential features of calculated $A(\omega)$ and differential conductance (dI/dV).

Actually, with our universal HEOM approach, the full spectrum of $A(\omega)$ can be obtained for any coupling strength t . As an example, Fig. S4 depicts the full spectral functions of a symmetric TIAM at $t = 0$ and $t = 2.0\Delta$, calculated by the HEOM approach at $L = 3$. The same set of parameters as that to plot Fig. 3 in the main text are adopted (in unit of Δ):

$\epsilon_1 = \epsilon_2 = -5$, $U_1 = U_2 = 10$, $W = 10$, and $T = 0.5$. The sum rule $\int_{-\infty}^{\infty} A(\omega) d\omega = 1$ is satisfied to numerical precision. One can see that the full spectrum resolves more resonance peaks at high frequency range, which provides rich information about the evolution of the energetic structure of the impurities system with the variation in t .

In Fig. S4, the three-peak-structure (the black line) at $t = 0$ is nothing but the duplication of the result for individual impurity, with the itinerant electrons screening the local spin moment at each impurity separately. At $t = 2.0 \Delta$ (the red line), the anti-ferromagnetic coupling ($J = 4t^2/U$) between the local spin moments splits the Kondo peak at $\omega = 0$. Meanwhile, the inter-impurity coupling t splits the high-frequency peaks at $\omega = \epsilon_d$ and $U + \epsilon_d$. Then, the three-peak structure of $A(\omega)$ changes to a six-peak one, as shown in Fig. S4. The details will be systematically studied in our future work.

C. Application to multi-impurity Anderson models

The HEOM approach is applicable to a general quantum impurity system, and the numerical procedures are easily extended to more complex systems than the single- and two-impurity Anderson models as discussed in Sec. III A and Sec. III B. To exemplify the applicability of the HEOM approach, we also perform calculations on a three-impurity Anderson model (3IAM) with the system Hamiltonian as follows,

$$H_{\text{sys}} = H_1 + H_2 + H_3 + V_{12} + V_{13} + V_{23}, \quad (\text{S42})$$

where $H_i = \sum_{\sigma} \epsilon_{i\sigma} \hat{a}_{i\sigma}^{\dagger} \hat{a}_{i\sigma} + U_i \hat{n}_{i\uparrow} \hat{n}_{i\downarrow}$ and $V_{ij} = t_{ij} (\hat{a}_{i\uparrow}^{\dagger} \hat{a}_{j\uparrow} + \hat{a}_{i\downarrow}^{\dagger} \hat{a}_{j\downarrow}) + \text{H.c.}$ Figure S8 exhibits the calculated system spectral functions of 3IAM for two cases: (i) $t_{12} = t_{13} = t_{23} = t = 0$, and (ii) $t_{12} = t_{23} = t \neq 0$ and $t_{13} = 0$. The variation of spectral density function induced by a small t is clearly demonstrated. In particular, it has been verified that in the case of $t = 0$, the calculated $A_i(\omega)$ for i th impurity in a 3IAM is exactly identical to $A(\omega)$ of a SIAM with its Hamiltonian taking the form of H_i . Note that Eq. (S42) is in a general form, and does not distinguish a degenerate case from a nondegenerate one. This infers that an impurity with high degeneracy (such as a transition metal atom with multiple d -electrons) is treated normally by the HEOM approach, without additional computational effort.

The computational cost of HEOM approach increases exponentially with the system size. The reason is mainly two-fold: (i) The system Hilbert space (spanned by Fock states) expands as 4^N , with N being the number of impurities. As a result, the system density matrix and each ADO in the hierarchy is a 4^N -by- 4^N matrix. (ii) The number of distinct exponential functions used to resolve the reservoir memory is $K = 2MN_{\mu}$, with N_{μ} being the number of impurities that are coupled to the reservoirs. Actually, in the present implementation of HEOM method, the major bottleneck is the physical memory required to store all the ADOs (rather than CPU time).

Fortunately, it is possible to improve substantially the efficiency of HEOM based on physical considerations and making use of the sparse nature of HEOM. This may extend

further the applicability of HEOM to more complex quantum impurity systems. First, the 4^N growth of system Fock space may be suppressed by imposing some physically reasonable constraint. For instance, with a rather large Coulomb repulsion strength (U_i), the double-occupancy Fock states may be omitted, which reduces the scaling to 3^N . Moreover, quite often some off-diagonal blocks of density matrix and ADOs are exactly zero, due to absence of quantum coherence between two Fock states. These blocks may be safely removed, and hence lead to saving of physical memory. For resolution of reservoir memory, an efficient filtering algorithm has been proposed by Shi *et al.* for bosonic bath environment,²¹ which performs a screening process to discard a large number of unimportant ADOs with negligible values, and hence reduces greatly the size of hierarchy while preserving the quantitative accuracy. Such kind of algorithms may be adopted to treat larger quantum impurity systems coupled to electron (fermionic) reservoirs, particular for the 5-band systems of significant experimental relevance.

IV. COMPARISON BETWEEN HEOM AND OTHER METHODS FOR QUANTUM IMPURITY SYSTEMS

In this section, we compare HEOM method and other methods frequently used for solving the Anderson impurity model, including numerical renormalization group (NRG), strong coupling continuous time quantum Monte Carlo (CTQMC), Green's function equation of motion (GFEOM), exact diagonalization (ED), slave-boson mean-field theory (SBMFT), and non-crossing approximation (NCA). For calculations discussed below, unless stated otherwise, the parameters for the Anderson impurity model are $\Delta = 0.02W$, $U = 3\pi\Delta$, $\epsilon_d = -U/2$, and temperature $T = 0.2\Delta$. Here $W = 1$ is the energy unit. Note that in the HEOM calculation, the energy unit is set as $W = 10$. It does not change the dimensionless results.

A. Comparison with numerical renormalization group method

The NRG method has been regarded as the most accurate method for solving impurity problems.²² This is because it can resolve exponentially small energy scales, thanks to the logarithmic discretization and iterative diagonalization algorithm. In order to make conclusive comparison with NRG and HEOM, we first need to produce accurate NRG data for the spectral function $A(\omega)$.

Here we use the full density matrix-NRG (FDM-NRG) method^{23,24} to produce $A(\omega)$ at a finite temperature. In order to get the most accurate spectral function, we combine FDM-NRG with the self-energy method of R. Bulla^{25,26} and the z-average method.^{27,28} For broadening the δ -functions in $A(\omega)$, we adopt the following scheme: A. Weichselbaum's log-Gaussian functions with width B_g are used for $|\omega| > \alpha T$;²³ while normal Gaussian functions

with width $B_{\text{zero}} = \alpha T$ are used for $|\omega| < \alpha T$. In our calculation, we use $N_z = 8$, $\alpha = 0.5$, and $B_g = 0.2$ which are found to minimize the broadening error.

Besides the broadening error, there are two sources of error in $A(\omega)$ from NRG. (1) Discretization error, usually described by how large the logarithmic discretization parameter Λ is ($\Lambda > 1$). This error disappears in the limit $\Lambda \rightarrow 1$. (2) Truncation error, described by how large the number of kept states M_s is. This error disappears in the limit $M_s \rightarrow \infty$. Therefore, the parameters that influences the accuracy of spectral function are Λ and M_s .

First, we examine the effect of decreasing Λ to approach 1 where discretization error disappears. In Fig. S9(a), we show $A(\omega)$ for different Λ , with relatively large M_s values for each Λ . Since the larger Λ is, the smaller M_s is required, we use different M_s for different Λ . As Λ decreases from 3.0 to 2.0, the weight in $A(\omega)$ transfers from the Hubbard peaks to the Kondo peak, leading to an increase of the height of Kondo peak and lower Hubbard peaks. As compared to HEOM curve, the overall agreement with HEOM is improved when Λ decreases.

Next, we examine the truncation error controlled by M_s . Note that the curves in Fig. S9(a) are not converged with respect to M_s . Now we fix $\Lambda = 2$ and increase M_s . It is seen from Fig. S9(b) that the curve for $M_s = [550, 580]$ are almost same as that of $M_s = [600, 630]$ in large frequency regime. The height of Kondo peak $A(0)$ converges as $M_s \rightarrow \infty$ in an oscillating way. It begins to converge from below for the largest number of kept states that we use, $M_s = [600, 630]$. We therefore believe that $\Lambda = 2.0$, $M_s = [600, 630]$ produces the best $A(\omega)$ within our efforts.

It is seen in Fig. S9(b) that the overall agreement between our best NRG result and HEOM is very good. $A(0)$ has about 4% relative error. For larger frequencies the relative error is less than 4%. Since the HEOM results are converged with respect to the level L while our NRG curve has not converged to $\Lambda = 1$, $M_s \rightarrow \infty$, we therefore conclude that in Fig. 1(b), the accuracy of $A(\omega)$ from HEOM is close to or higher than the best NRG result that we obtain. To reach such a comparable accuracy, the calculation time of NRG and HEOM are also comparable, both are of the order of a few hours on a workstation.

B. Comparison with continuous time quantum Monte Carlo method

CTQMC is in principle exact, provided that there is no minus sign problem and the number of sampling tends to infinity.²⁹ Here we compare the spectral function from HEOM and the strong coupling CTQMC calculations. For CTQMC, the imaginary time Green's function $G(\tau)$ is first calculated. The spectral function $A(\omega)$ is then produced by the maximum entropy method.³⁰ The transform of information from $G(\tau)$ to $A(\omega)$ is an numerically ill-posed problem. We find that the resulting spectral function depends rather sensitively on the statistical distribution of the input $G(\tau)$, which is controlled by parameters of CTQMC, such as nsweep (number of sweeps), ntimes (number of discrete τ 's), and iwmax (number of

Matsubara frequencies of input $\Delta(i\omega_n)$.

This makes the error bars of $A(\omega)$ much larger than the statistical error bars of $G(\tau)$. In Fig. S10(a), we plot $A(\omega)$ from CTQMC with different control parameters and compare them with those from HEOM and NRG. It is seen that for these sets of parameters, the variation of $\pi\Delta A(\omega)$ is 4×10^{-2} around the Hubbard peaks, even though the statistical errors of all the $G(\tau)$'s are already smaller than 6×10^{-4} . Compared to HEOM result, the maximum relative error in $A(\omega)$ is about 15%, mainly in the intermediate frequency regime. To elucidate the source of discrepancy, we calculate $G(\tau)$ from $A(\omega)$ of HEOM and compare it with the $G(\tau)$ directly from CTQMC. As shown in Fig. S10(b), they agree much better, with the maximum relative error of 5% at $\tau = \beta/2$.

Therefore, we conclude that although $G(\tau)$ agrees well between CTQMC and HEOM, it is difficult to achieve quantitatively converged spectral function $A(\omega)$ by CTQMC approach, due to the large uncertainties associated with the analytical continuation of Green's function to real energies with the maximum entropy method.

C. Comparison with refined Green's function equation of motion method

Various equations of motion (EOM) methods using many-particle Green's functions (GFs) or density operators as basic variables had been developed.³¹ However, very few method of this kind is able to address strong correlation effects in quantum impurity system. Luo *et al.* have proposed a refined GF-EOM method,³² which yields $A(\omega)$ of a SIAM in the Kondo regime comparable to that by NRG method; see Fig. 2 of Ref. [32]. It is important to clarify that our HEOM approach is distinctly different from the refined GF-EOM method of Luo *et al.* (and many others) in terms of fundamental formalism, practical implementation, and overall performance.

1. Difference in fundamental formalism

The GF-EOM method of Ref. [32] uses many-body GFs as basic variables, and the complete set of equations involves explicitly all the single-electron states of the reservoirs (labeled by k -index). It treats the system and reservoir degrees of freedom on the same footing. This inevitably leads to a rather large number of GFs to solve, even at a low level of hierarchy. In contrast, our HEOM method uses reduced density matrix and auxiliary density operators as basic variables. It is only the reduced system (impurities) that is treated explicitly, and the influence of electron reservoir of infinite degrees of freedom is accounted for by statistical means. The only information required for the reservoir is its memory content, which can be decomposed efficiently into a number of characteristic dissipative modes. Consequently, our HEOM method involves much fewer unknowns than the GF-EOM, due to the statistical treatment for the electron reservoir.

2. *Difference in practical implementation*

Another key difference is that in our HEOM method the couplings among different auxiliary density operators are determined systematically from the Feynmann–Vernon path integral formalism,¹ and hence the HEOM can be cast into a generic compact form; see Eq. (1) of main text. As a consequence, our HEOM method is applicable to more complex quantum impurity systems such as multi-impurity and multi-reservoir models without additional derivation effort. In contrast, the extension of present GF–EOM method is much more tricky, because the EOM of each individual GF requires analytic derivation, and the complexity increases drastically as the model becomes more complicated.

Furthermore, in our HEOM method the truncation of hierarchy is carried out in a systematic way, so that it is easy to verify the numerical convergence of resulting data with respect to truncation level. In contrast, the present GF–EOM method is hampered by lacking a general recipe for truncation. In most of calculations, the truncation scheme is strongly empirical and rather arbitrary. Therefore, it cannot be regarded as a controlled approximate method. In the work of Luo *et al.*,³² a formal criterion is introduced to guide the truncation, but still with the use of empirical approximations to simplify the calculations.

3. *Difference in overall performance*

As demonstrated in our manuscript, the spectral functions resulted from our HEOM approach agrees quantitatively with those calculated with the latest state-of-the-art NRG method. On the other hand, to the best of knowledge, the most accurate GF–EOM method produces only qualitatively correct results for the Anderson impurity model. As shown in Fig. 2 of Ref. [32], for temperatures $T < T_K$, the relative deviation in $A(\omega = 0)$ is about 20%. In contrast, the HEOM results has a relative deviation less than 4% when compared with our best NRG result. Therefore, it is apparent that HEOM generally outperforms the sophisticated GF–EOM calculation in accuracy.

D. Comparison with exact diagonalization method

The ED method is an important numerical method for solving many-body problems with limited degrees of freedom.³³ It is often used as an impurity solver in the context of dynamical mean-field theory.^{34–36} As shown in Figs. 1 and 2 in the main text, the HEOM approach can produce a smooth spectral function similar to NRG by treating all reservoir degrees of freedom in a statistical manner. In contrast, the ED method uses a finite number (N_b) of single-particle states to represent the electron reservoir. Limited by computer memory, usually the adopted N_b is not a very large number, which might lead to strong quantum confinement effect, due to the finite size of Hilbert space. In practice, $N_b \leq 9$ is adopted for

a full diagonalization algorithm, and a somewhat larger $N_b \sim 15$ is feasible with the Lanczos algorithm for ground-state properties at zero temperature.^{37,38}

Figure S11 shows the ED results for $U = 3.0\pi\Delta$ using $N_b = 7$ bath sites, with V_k 's and ϵ_k 's fitted from the hybridization function $\Delta(i\omega_n)$. Here, an odd number of bath sites is adopted to properly describe the noninteracting electron reservoirs.³⁹ As shown in Fig. S11, the Kondo peak and the Hubbard peaks are resolved qualitatively by the ED method, but the Kondo peak is composed of two small peaks with a splitting due to finite size effect. The positions of the Hubbard peaks are close to $\pm U/2$, but their widths are smaller than the HEOM results. This ED calculation takes about five hours in our workstation, consumed mainly by the calculation of the density of states. Such computational time is on the same order of magnitude as the time of HEOM calculation shown in Table S1 and S2. Thus we conclude that with similar computational cost, HEOM has much higher energy resolution than ED.

E. Comparison with slave-boson mean field theory and non-crossing approximation

Both SBMFT and NCA are analytical approximation methods. In this section, we compare their results with HEOM.

The Kotliar–Ruckenstein SBMFT⁴⁰ is a convenient theory to study the Anderson impurity model with finite U . It can qualitatively describe features of the Fermi-liquid ground state, such as the quasi-particle weight z and the Kondo resonance peak in the spectral function $A(\omega)$. The spectral function from SBMFT is expressed as (for paramagnetic and particle-hole symmetric case),

$$A(\omega) = -\frac{1}{\pi} \text{Im} \frac{z}{\omega + i\eta - z\Gamma(\omega + i\eta)}. \quad (\text{S43})$$

Here, z is the quasi-particle weight, determined by a mean-field equation. $\Gamma(\omega + i\eta)$ is the Kramers–Kronig transformation of the hybridization function $\Delta(\omega)$. Therefore, $A(\omega)$ has the form of non-interacting density of states, but renormalized by the factor z .

In Fig. S12, we compare $A(\omega)$ from SBMFT and HEOM at a finite temperature $T = 0.2\Delta$. In Fig. S12(a), it is seen that the Hubbard peaks at $\omega = \pm U/2$ are missing in $A(\omega)$ of SBMFT. This is because SBMFT does not correctly describe the temporal quantum fluctuations on the impurity site. The total weight of $A(\omega)$ only contains the Fermi liquid quasi-particle weight z which decrease from 1 as U increases. In the inset of Fig. S12(a), SBMFT and HEOM spectral function are compared for $U = 0.5\pi\Delta$. They agree quite well because for such a small U , there is no local moment formation and the renormalized Fermi liquid description is valid.

Another feature of $A(\omega)$ in Fig. S12(a) is that the height of Kondo peak $A(0)$ does not change with U . This is a feature of Fermi liquid phase at $T = 0$, but should not hold for the finite temperature that we study here. This shows that for finite temperature, SBMFT

cannot correctly describe the suppression the Kondo peak by the thermal fluctuation, while it is correctly described in the HEOM results shown in Fig.S12(b).

NCA is based on the partial summation of the diagrams in the perturbative expansion of hybridization function under the slave-boson representation. Complementary to SBMFT, NCA can handle the high energy features such as the Hubbard peaks, but fails to describe the Fermi liquid features in the low energy regime, such as the Kondo peak at temperatures $T < T_K$ (Ref. 41). In contrast, HEOM not only correctly produces the Hubbard peaks, but also produces accurate Kondo peaks at the low temperature $T = 0.2\Delta < T_K$, as shown in the main text.

We conclude that both SBMFT and NCA work only in limited regime of the parameter space, while HEOM applies to much wider area of the parameter space, covering both low and high energies.

-
- * Electronic address: xz58@ustc.edu.cn
† Electronic address: wjh@ruc.edu.cn
‡ Electronic address: yyan@ust.hk
- ¹ R. P. Feynman and F. L. Vernon, Jr., *Ann. Phys.* **24**, 118 (1963).
 - ² H. Kleinert, *Path Integrals in Quantum Mechanics, Statistics, Polymer Physics, and Financial Markets*, World Scientific, Singapore, 2009, 5th ed.
 - ³ R. X. Xu, P. Cui, X. Q. Li, Y. Mo, and Y. J. Yan, *J. Chem. Phys.* **122**, 041103 (2005).
 - ⁴ R. X. Xu and Y. J. Yan, *Phys. Rev. E* **75**, 031107 (2007).
 - ⁵ J. S. Jin, X. Zheng, and Y. J. Yan, *J. Chem. Phys.* **128**, 234703 (2008).
 - ⁶ X. Zheng, J. S. Jin, S. Welack, M. Luo, and Y. J. Yan, *J. Chem. Phys.* **130**, 164708 (2009).
 - ⁷ A. Croy and U. Saalman, *Phys. Rev. B* **80**, 073102 (2009).
 - ⁸ J. Hu, R. X. Xu, and Y. J. Yan, *J. Chem. Phys.* **133**, 101106 (2010).
 - ⁹ J. Hu, M. Luo, F. Jiang, R. X. Xu, and Y. J. Yan, *J. Chem. Phys.* **134**, 244106 (2011).
 - ¹⁰ X. Zheng, J. S. Jin, and Y. J. Yan, *J. Chem. Phys.* **129**, 184112 (2008).
 - ¹¹ X. Zheng, J. S. Jin, and Y. J. Yan, *New J. Phys.* **10**, 093016 (2008).
 - ¹² X. Zheng, J. Y. Luo, J. S. Jin, and Y. J. Yan, *J. Chem. Phys.* **130**, 124508 (2009).
 - ¹³ R. W. Freund and N. M. Nachtigal, *SIAM J. Numer. Math.* **60**, 315 (1991).
 - ¹⁴ R. W. Freund, *SIAM J. Sci. Comput.* **14**, 470 (1993).
 - ¹⁵ W. H. Press, S. A. Teukolsky, W. T. Vetterling, and B. P. Flannery, *Numerical Recipes in Fortran*, Cambridge University Press, New York, 1992.
 - ¹⁶ R. Kosloff, *J. Phys. Chem.* **92**, 2087 (1988).
 - ¹⁷ A. C. Hewson, *The Kondo Problem to Heavy Fermions*, Cambridge University Press, Cambridge, 1993.
 - ¹⁸ R. Žitko and J. Bonča, *Phys. Rev. B* **74**, 045312 (2006).

- ¹⁹ H. R. Krishna-murthy, J. W. Wilkins, and K. G. Wilson, Phys. Rev. B **21**, 1044 (1980).
- ²⁰ N. L. Dickens and D. E. Logan, J. Phys.: Condens. Matter **13**, 4505 (2001).
- ²¹ Q. Shi, L. P. Chen, G. J. Nan, R. X. Xu, and Y. J. Yan, J. Chem. Phys. **130**, 084105 (2009).
- ²² K. G. Wilson, Rev. Mod. Phys. **47**, 773 (1975).
- ²³ A. Weichselbaum and J. von Delft, Phys. Rev. Lett. **99**, 076402 (2007).
- ²⁴ R. Peters, T. Pruschke, and F. B. Anders, Phys. Rev. B **74**, 245114 (2006).
- ²⁵ R. Bulla, A. C. Hewson, and T. Pruschke, J. Phys.: Condens. Matter **10**, 8365 (1998).
- ²⁶ R. Bulla, Phys. Rev. Lett. **83**, 136 (1999).
- ²⁷ M. Yoshida, M. A. Whitaker, and L. N. Oliveira, Phys. Rev. B **41**, 9403 (1990).
- ²⁸ W. C. Oliveira and L. N. Oliveira, Phys. Rev. B **49**, 11986 (1994).
- ²⁹ E. Gull et al., Rev. Mod. Phys. **83**, 349 (2011).
- ³⁰ In this work, we used the CTQMC and maximum entropy code from Liang Du, Li Huang and Xi Dai through private communication.
- ³¹ J. N. Pedersen and A. Wacker, Phys. Rev. B **72**, 195330 (2005).
- ³² H.-G. Luo, J.-J. Ying, and S.-J. Wang, Phys. Rev. B **59**, 9710 (1999).
- ³³ E. Dagotto, Rev. Mod. Phys. **66**, 763 (1994).
- ³⁴ M. Caffarel and W. Krauth, Phys. Rev. Lett. **72**, 1545 (1994).
- ³⁵ Q. Si, M. J. Rozenberg, G. Kotliar, and A. E. Ruckenstein, Phys. Rev. Lett. **72**, 2761 (1994).
- ³⁶ A. Georges, G. Kotliar, W. Krauth, and M. J. Rozenberg, Rev. Mod. Phys. **68**, 13 (1996).
- ³⁷ M. Capone, L. de' Medici, and A. Georges, Phys. Rev. B **76**, 245116 (2007).
- ³⁸ A. Liebsch and H. Ishida, J. Phys.: Condens. Matter **24**, 053201 (2012).
- ³⁹ M. J. Rozenberg, G. Moeller, , and G. Kotliar, Mod. Phys. Lett. B **8**, 535 (1994).
- ⁴⁰ G. Kotliar and A. E. Ruckenstein, Phys. Rev. Lett. **57**, 1362 (1986).
- ⁴¹ N. E. Bickers, Rev. Mod. Phys. **59**, 845 (1987).

L	# of unknowns	Memory (MB)	CPU time (s)	n_d
1	352	0.1	1.6	0.49156
2	4,512	0.4	1.6	0.47980
3	29,152	2.0	2.3	0.47602
4	188,032	13.0	8.4	0.47650
5	868,096	59.7	39.7	0.47649
6	3,920,896	269.3	239.9	0.47649

Table S1: Summary of HEOM calculations on an SIAM with the parameters of (in unit of Δ): $T = 1.5$, $\epsilon_d = -5$, $U = 15$, $W = 10$, and $\Delta_L = \Delta_R = 0.5$. The number of occupied electrons on the impurity (per spin), $n_d = \text{tr}_s(\hat{n}_\mu \rho_{\text{eq}})$, is calculated at various truncation tiers (up to $L = 6$). The number of unknowns, computer memory, and CPU time are listed for each L . The converged digits of the resulting n_d are highlighted with boldface at each L . A total number of 4 Padé points are sufficient to reproduce the reservoir correlation function quantitatively. Calculations are done on a single PC with a 4-core 2.8 GHz Intel(R) Core(TM) i5-2300 CPU.

L	# of unknowns	Memory (MB)	CPU time (s)	n_d
1	1,056	0.1	1.6	0.50000
2	42,528	3.0	3.1	0.49163
3	774,688	53.2	53.4	0.47832
4	14,678,816	1008.0	1252.3	0.48224
5	67,721,088	4650.1	9004.9	0.48226

Table S2: Summary of HEOM calculations on an SIAM with the parameters of (in unit of Δ): $T = 0.075$, $\epsilon_d = -5$, $U = 15$, $W = 10$, and $\Delta_L = \Delta_R = 0.5$. The number of occupied electrons on the impurity (per spin), $n_d = \text{tr}_s(\hat{n}_\mu \rho_{\text{eq}})$, is calculated at various truncation tiers (up to $L = 5$). The number of unknowns, computer memory, and CPU time are listed for each L . A total number of 15 Padé points are used to reproduce the reservoir correlation function at all L , except for $L = 5$ where 12 Padé points are used. Calculations are done on a single PC with a 4-core 2.8 GHz Intel(R) Core(TM) i5-2300 CPU.

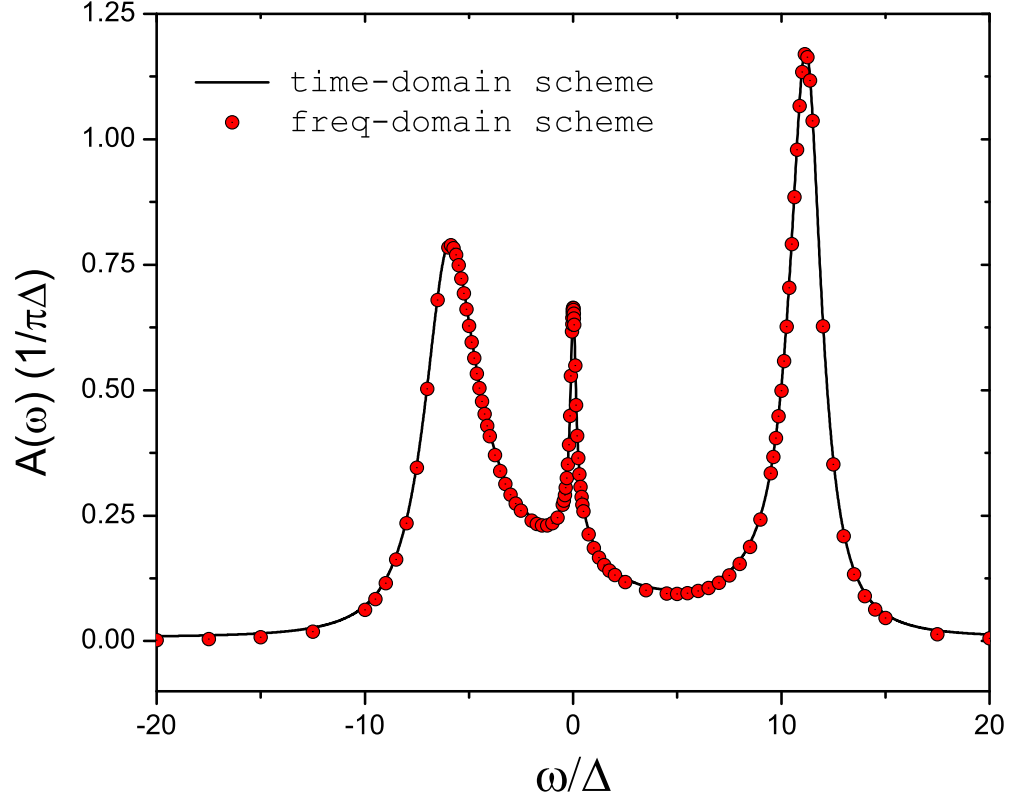


Figure S1: Spectral function of an asymmetric SIAM calculated by the HEOM approach at $L = 4$. The same set of parameters as that used for plotting Fig. 1 in the main text are adopted here (in unit of Δ): $\epsilon_d = -5$, $U = 15$, $W = 10$, and $T = 0.075$. The results of both time-domain and frequency-domain schemes are displayed.

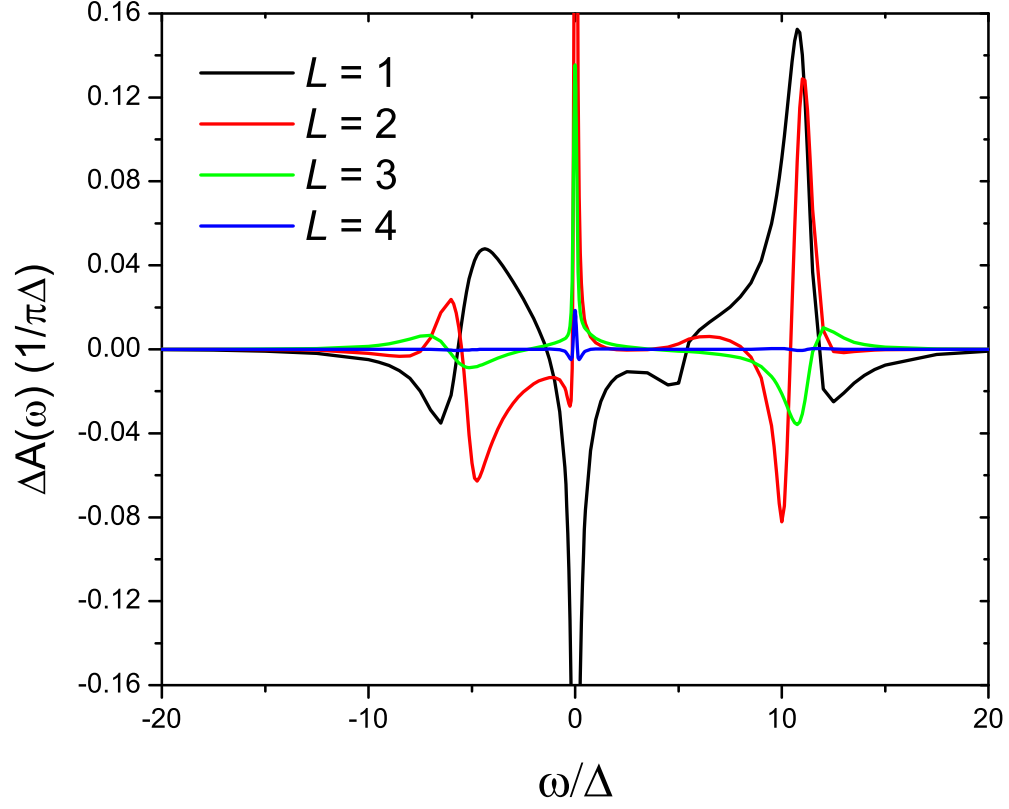


Figure S2: Deviation of system spectral function of an asymmetric SIAM calculated at $L = 1 \sim 4$ from the $L = 5$ result. The same set of parameters as that used for plotting Fig. 1 in the main text are adopted here (in unit of Δ): $\epsilon_d = -5$, $U = 15$, $W = 10$, and $T = 0.075$.

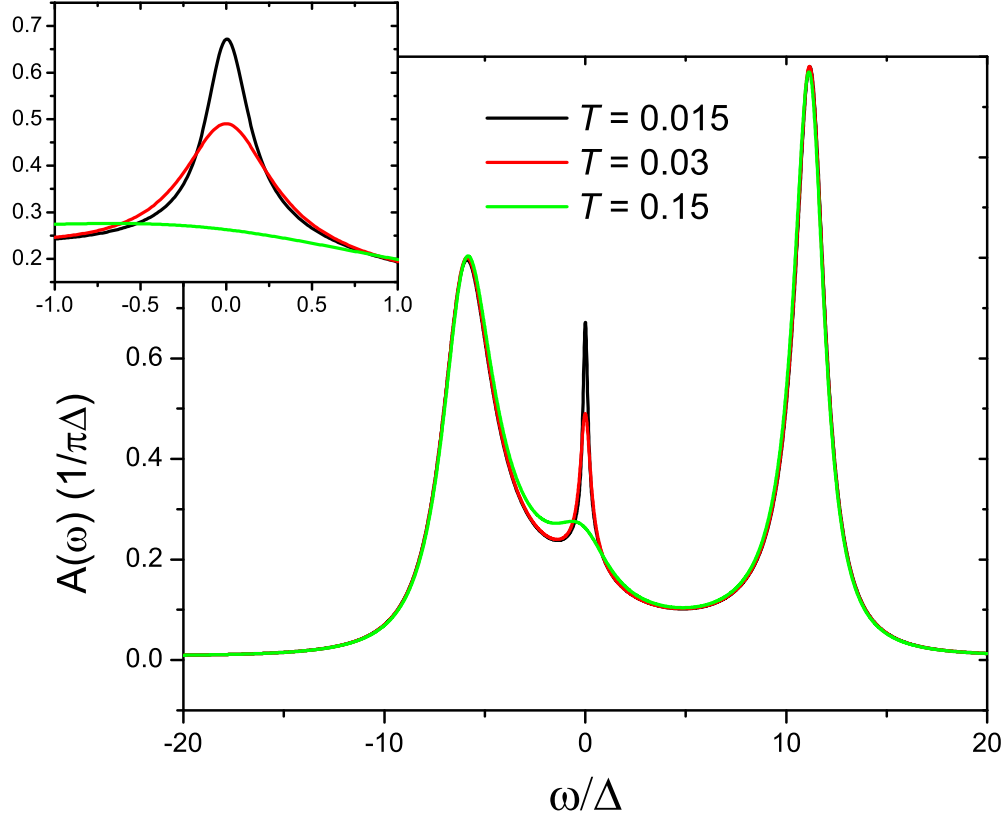


Figure S3: Calculated system spectral function of an asymmetric SIAM at different temperatures. The same set of parameters as that used for plotting Fig. 1 in the main text are adopted here (in unit of Δ): $\epsilon_d = -5$, $U = 15$, $W = 10$, and $T = 0.075$. All curves are obtained at $L = 5$, and are considered to be quantitatively converged. The inset magnifies the low frequency range where the Kondo resonance peak becomes more prominent at a lower temperature.

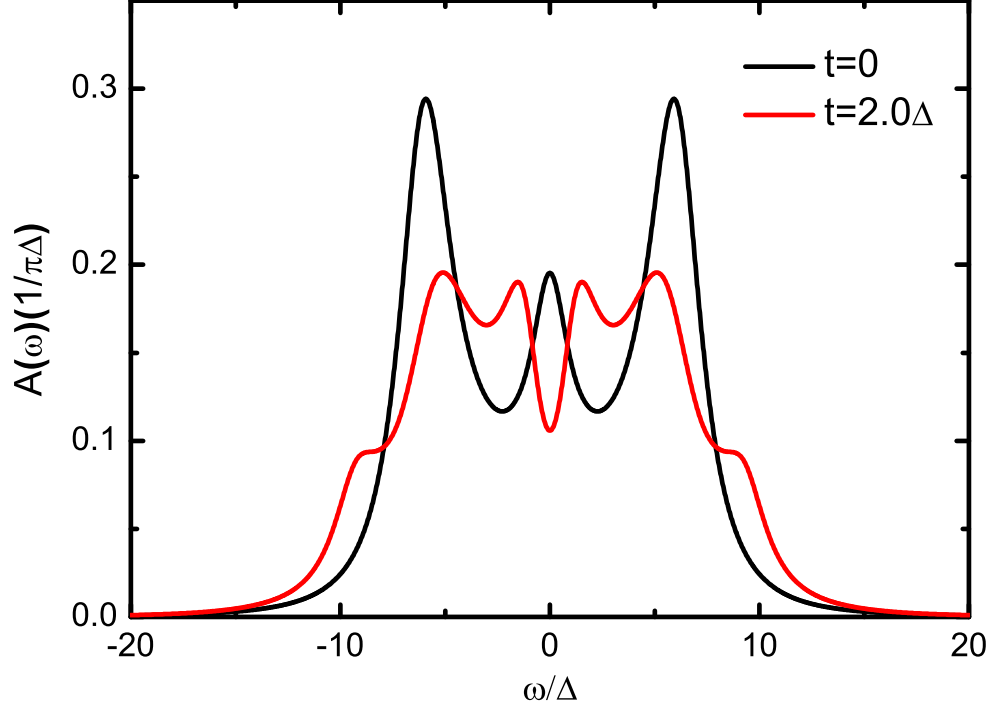


Figure S4: The full spectral function of a symmetric TIAM calculated by the HEOM approach at $L = 3$. The same set of parameters as that adopted for plotting Fig. 3 in the main text are considered here (in unit of Δ): $\epsilon_1 = \epsilon_2 = -5$, $U_1 = U_2 = 10$, $W = 10$, and $T = 0.5$.

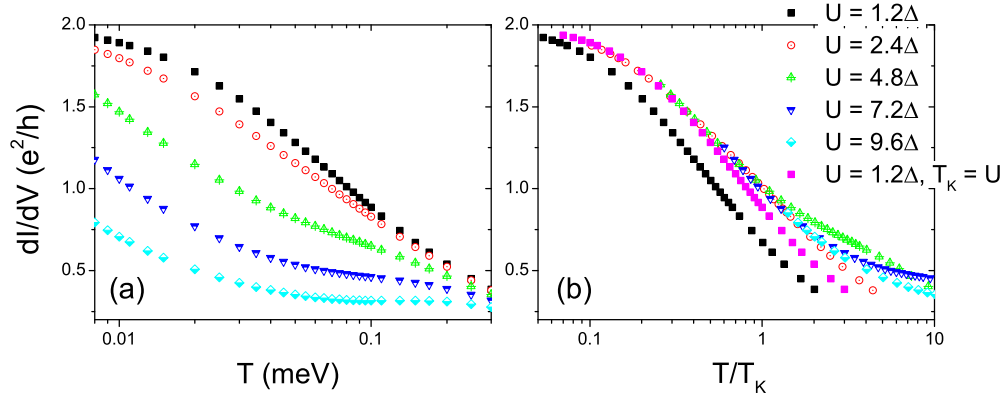


Figure S5: Zero-bias differential conductance (in unit of e^2/h) versus (a) unscaled and (b) T_K -scaled temperatures, for symmetric SIAM systems of different values of $U = -2\epsilon_d$. The Kondo temperature T_K is evaluated with Eq. (S39), except for the pink squares in (b) where U is taken as the Kondo energy scale and used to scale the temperature. Other parameters are (in unit of meV): $W = 2$ and $\Delta = 0.0833$. Calculations are done with the HEOM approach with $L = 4$.

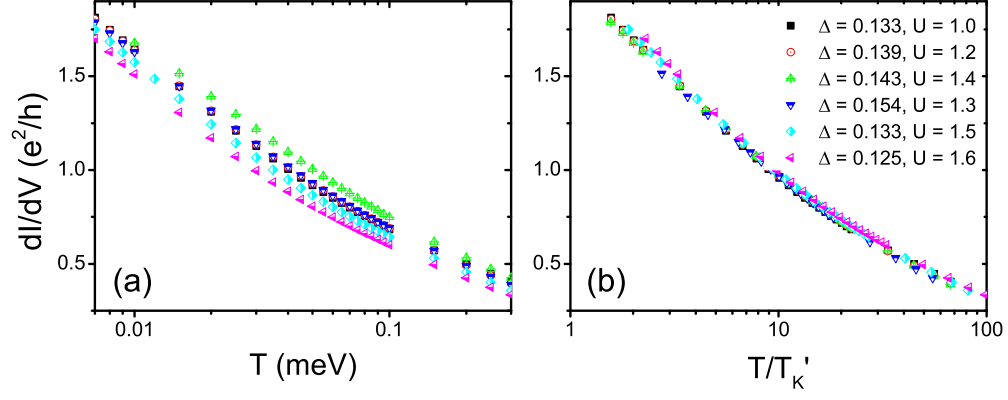


Figure S6: Zero-bias differential conductance (in unit of e^2/h) versus (a) unscaled and (b) T'_K -scaled temperatures, for asymmetric SIAMs of different U and Δ in unit of meV. The Kondo temperature T'_K is calculated with Eq. (S40). Other parameters are (in unit of meV): $W = 2$, and $\epsilon_d = -0.2$. Calculations are done with the HEOM approach with $L = 4$.

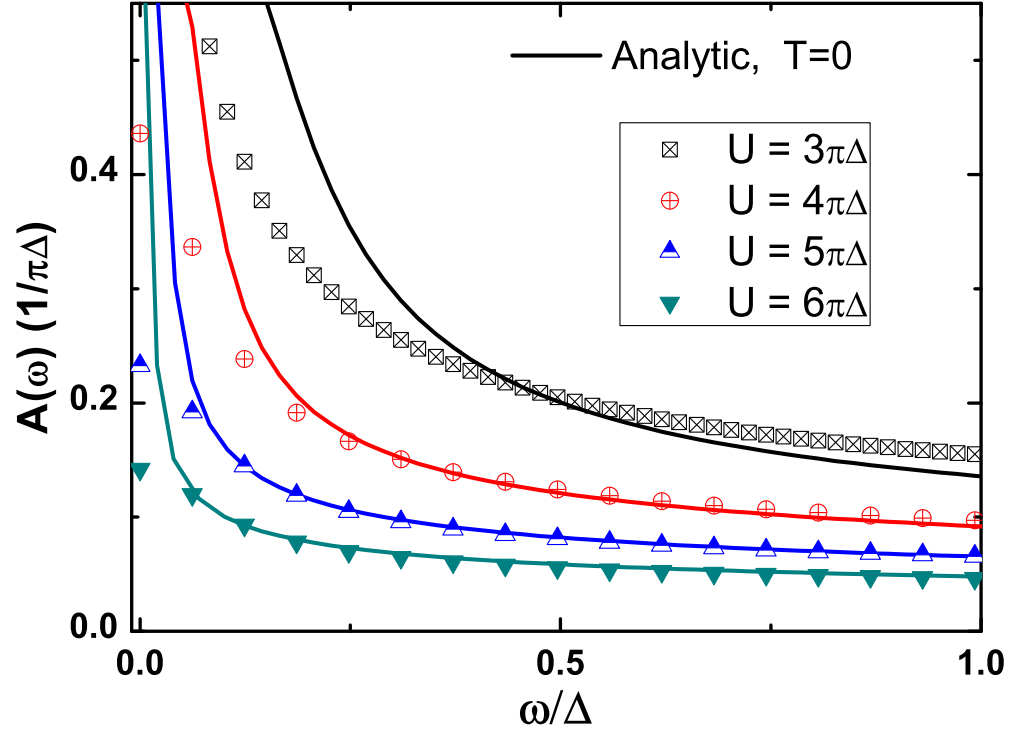


Figure S7: Spectral functions of symmetric SIAMs of various values of U . The scattered data are the HEOM numerical results, while the solid curves follow the analytic expression of Eq. (S41). Other parameters adopted in the HEOM calculations are: $W = 50\Delta$ and $T = 0.05\Delta$.

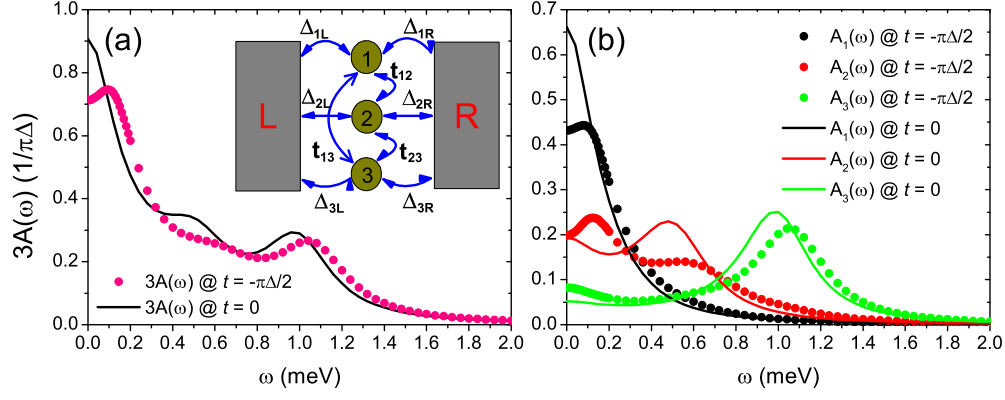


Figure S8: Spectral functions of a three-impurity Anderson model system sketched in the inset of (a). Panels (a) and (b) depict the spectral function of total system $3A(\omega) = \sum_i A_i(\omega)$ and that of i th impurity $A_i(\omega)$, respectively. The inter-impurity coupling strengths are set to $t_{12} = t_{23} = t$ and $t_{13} = 0$, *i.e.*, only the nearest neighboring impurities are considered to be coupled. The lines and circles correspond to $t = 0$ and $t = -\pi\Delta/2$, respectively. Other system parameters are: $U_1 = -2\epsilon_1 = \pi\Delta$, $U_2 = -2\epsilon_2 = 3\pi\Delta$, $U_3 = -2\epsilon_3 = 6\pi\Delta$, $T = 0.75\Delta$, $W = 50\Delta$, and $\Delta = 0.1$ meV. Calculations are done with the HEOM approach with $L = 3$.

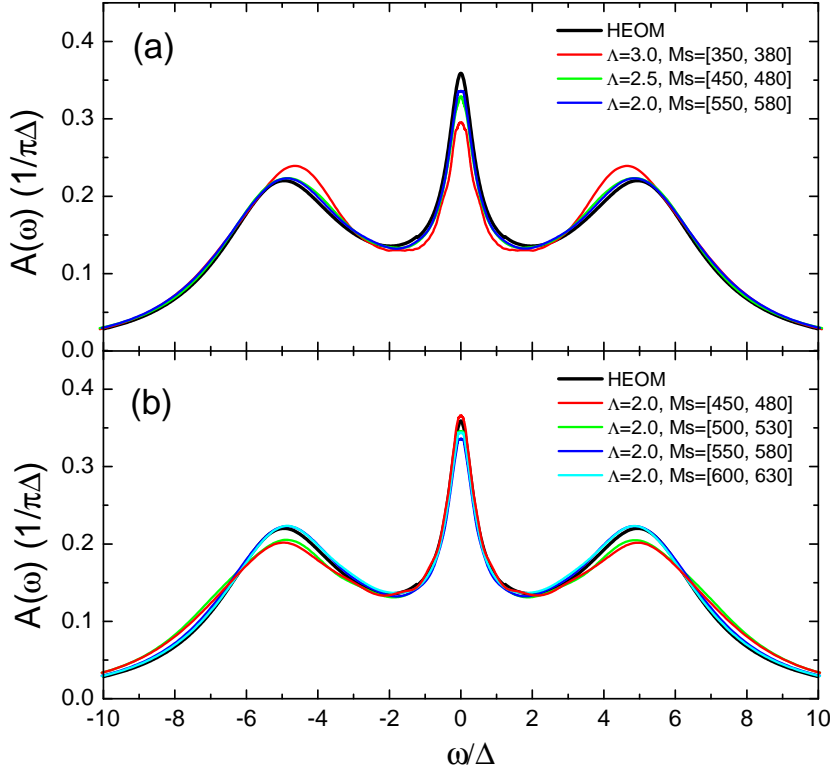


Figure S9: (a) $A(\omega)$ from NRG using different Λ (red, green, and blue lines). For each Λ , we choose a relatively large M_s . (b) $A(\omega)$ from NRG with $\Lambda = 2.0$ and different M_s (red, green, blue, and cyan lines). In both (a) and (b), HEOM curve is also shown for comparison (black line). The parameters are $\Delta = 0.02W$, $U = 3\pi\Delta$, $\epsilon_d = -U/2$, and temperature $T = 0.2\Delta$. W is the energy unit.

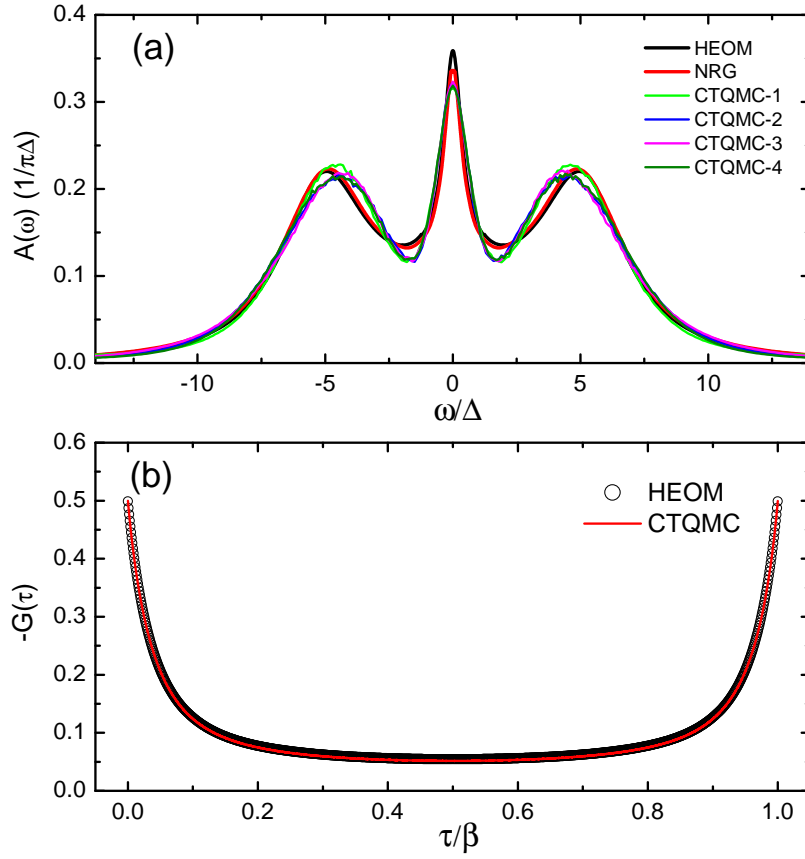


Figure S10: (a) Comparison of spectral function from HEOM (black line), NRG (red line), and the strong coupling CTQMC (lines with other colors). The parameters for CTQMC-1 to CTQMC-4 are: $(\text{nsweep}, \text{ntimes}, \text{iwmax}) = (6 \times 10^9, 2^{10}, 2^{22}), (2.4 \times 10^{10}, 2^{11}, 2^{19}), (6 \times 10^9, 2^{13}, 2^{22}),$ and $(9.1 \times 10^{11}, 2^{13}, 2^{23})$, respectively. (b) Comparison of $G(\tau)$ between HEOM (black circle) and CTQMC (red line). The CTQMC data is obtained using the parameter of the CTQMC-4 in (a). Other parameters are $\Delta = 0.02W$, $U = 3\pi\Delta$, $\epsilon_d = -U/2$, and temperature $T = 0.2\Delta$. W is the energy unit.

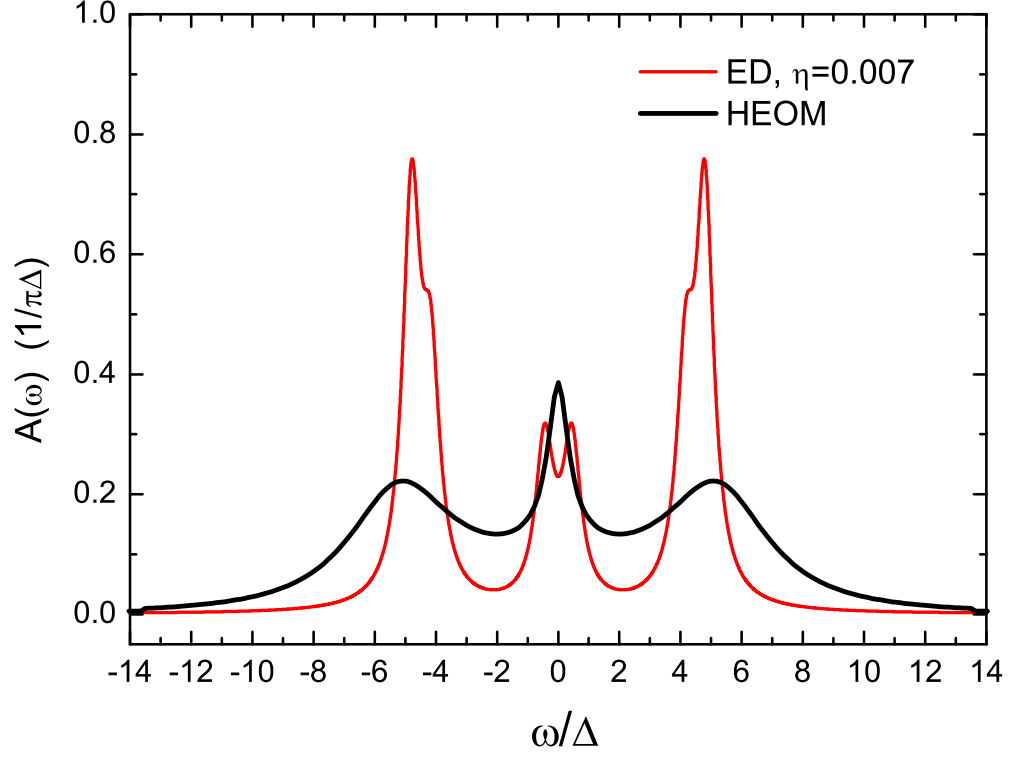


Figure S11: Comparison of ED and HEOM spectral function. $A(\omega)$ from ED ($N_b = 7$) is broadened with Lorentzian function of width $\eta = 0.007$. The parameters are $\Delta = 0.02W$, $U = 3.0\pi\Delta$, $\epsilon_d = -U/2$, and temperature $T = 0.2\Delta$. W is the energy unit.

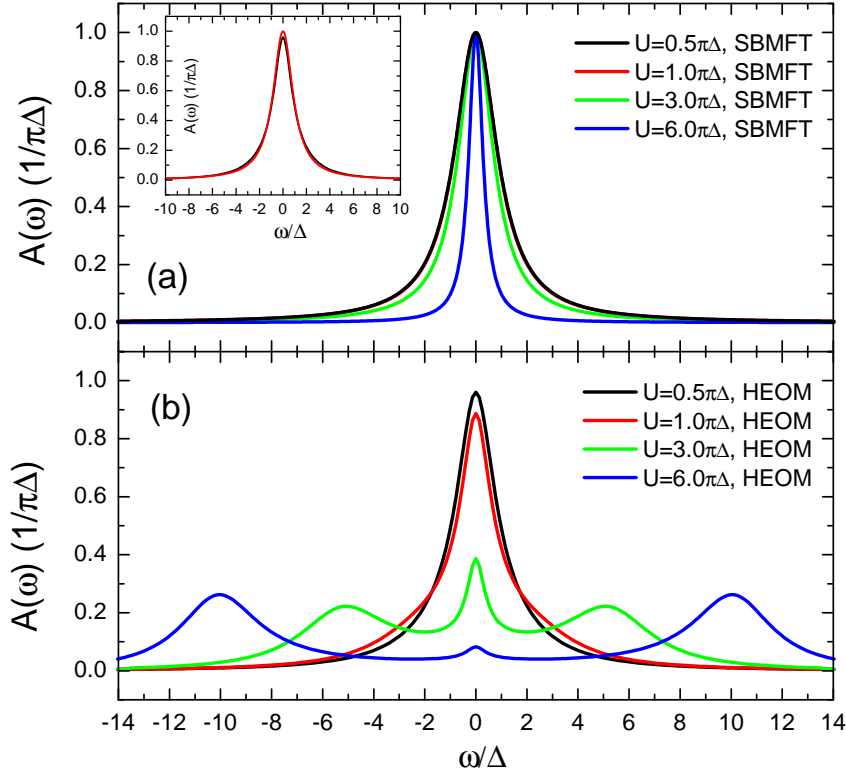


Figure S12: (a) $A(\omega)$ from SBMFT for different U 's. Inset: comparison of SBMFT (red line) and HEOM (black line) result for $U = 0.5\pi\Delta$. (b) $A(\omega)$ from HEOM for different U . For (a) and (b), other parameters are $\Delta = 0.02W$, $\epsilon_d = -U/2$, and temperature $T = 0.2\Delta$. W is the energy unit.